Published in final edited form as:

ACS Catal. 2019 July 5; 9(7): 5847–5859. doi:10.1021/acscatal.9b00360.

Redesign of a Copper Storage Protein into an Artificial Hydrogenase

Dhanashree Selvan[⊥,±], **Pallavi Prasad**[⊥,±], **Erik R. Farquhar**[≠], **Yelu Shi**[ξ], **Skyler Crane**[⊥], **Yong Zhang**[ξ], **Saumen Chakraborty**[⊥,*]

[⊥]Department of Chemistry and Biochemistry, University of Mississippi, University, MS 38677, USA.

[≠]Case Western Reserve University Center for Synchrotron Biosciences, NSLS-II, Brookhaven National Laboratory, Upton, NY 11973, USA.

[ξ]Department of Chemistry and Chemical Biology, Stevens Institute of Technology, 1 Castle Point on Hudson, NJ 07030, USA.

Abstract

We report the construction of an artificial hydrogenase (ArH) by reengineering a Cu storage protein (Cspl) into a Ni-binding protein (NBP) employing rational metalloprotein design. The hypothesis driven design approach involved deleting existing Cu sites of Csp1 and identification of a target tetrathiolate Ni binding site within the protein scaffold followed by repacking the hydrophobic core. Guided by modeling, the NBP was expressed and purified in high purity. NBP is a well-folded and stable construct displaying native-like unfolding behavior. Spectroscopic and computational studies indicated that the NBP bound nickel in a distorted square planar geometry that validated the design. Ni(II)-NBP is active for photo-induced H_2 evolution following a reductive quenching mechanism. Ni(II)-NBP catalyzed H^+ reduction to H_2 gas electrochemically as well. Analysis of the catalytic voltammograms established a proton-coupled electron transfer (PCET) mechanism. Electrolysis studies confirmed H_2 evolution with quantitative Faradaic yields. Our studies demonstrate an important scope of rational metalloprotein design that allows imparting functions into protein scaffolds that have natively not evolved to possess the same function of the target metalloprotein constructs.

Graphical Abstract

[*]Corresponding Author: saumenc@olemiss.edu.
[±]D.S. and P.P. contributed equally.

Supporting Information. The supporting information is available at the ACS Publications website free of charge. Relevant Q M M M summary, gene sequence of NBP, design overview, structural synopsis of Csp1, PAGE, SEC, MALDI, thermal melt, UV-vis titration, photographs of protein-metal solutions, deconvoluted EXAFS fit, QM models of $NiCys_4$, GC traces, Stern-Volmer analysis, UV-vis, CD, MALDI before and after CPE, and relevant data Tables.

The authors declare no competing financial interest

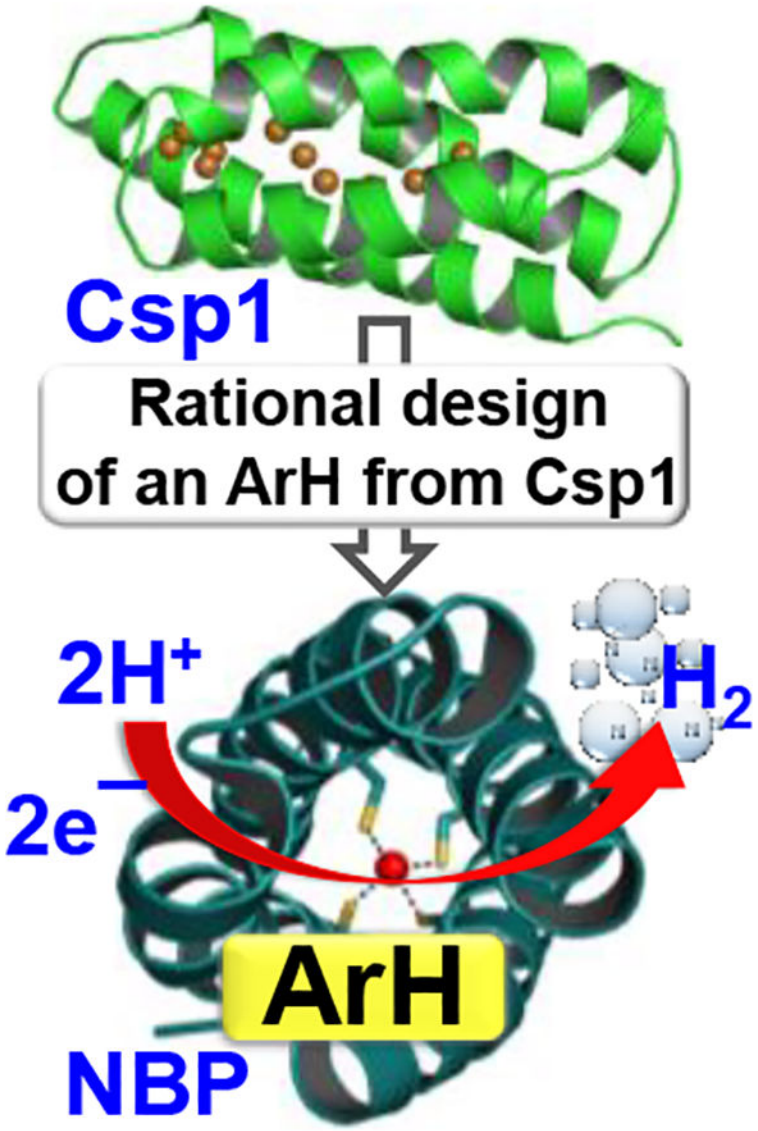

Keywords

Protein design; artificial metalloenzymes; hydrogenases; spectroscopy; catalysis

INTRODUCTION:

Design of artificial metalloenzymes (ArMs) is an approach that allows structure guided construction of metalloproteins inspired by native enzymes. Such endeavors rely upon a thorough understanding of the active site structure and the surrounding protein matrix that position the metal coordinating residues in specific spatial orientations. The ArMs can not only serve as simpler structural and functional models of native enzymes; they also offer simplified view of the reaction mechanism. The knowledge gained from the design process enables construction of ArMs with novel structures and functions for applications ranging

from healthcare to alternate energy. Hydrogenases hold promise in alternate energy technology by producing H_2 gas as a potential transportation fuel, in H_2 fuel cells, and as an ingredient for the Haber-Bosch process. However the innate complexity of the enzyme and low yields hinder realization of these dreams.[1–2] Development of artificial hydrogenases (ArHs) via rational metalloprotein design as "simpler" functional models that are robust and can function under environmentally benign conditions, is one avenue to alleviate these challenges and sustain a carbon neutral energy economy for the future.

Hydrogenases catalyze reversible $2e^-$ interconversion between H_2 gas and protons [H_2 ($\leftrightarrows$ $H^+ + H^-$) $\leftrightarrows$ $2H^+ + 2e^-$].[3] These enzymes produce energy for certain organisms and balance cellular redox potentials. Depending on location in the cell, hydrogenases can either produce H 2 by removing reducing equivalents or oxidize H_2 and produce electrons. Among three common classes of hydrogenases, the [NiFe] hydrogenases feature a heterobimetallic active site containing two bridged Cys thiolate ligands shared between the Ni and Fe (Figure 1).[2–7] Two terminal Cys residues ligated to Ni and an open site for substrate binding and activation complete the square pyramidal geometry of the Ni site. In addition to the bridged thiolates the octahedral Fe site is also coordinated to one CO and two CN^- ligands. The reactivity of the enzyme is further facilitated by the presence of a base nearby. Biophysical studies have shown that the soft thiolate ligands influence the spin and charge density of the metal sites, thus, tuning the electronic properties of the active site.[2–6] Electron transfer (ET) to the deeply buried active site is accomplished by the presence of three Fe-S clusters. There are also dedicated proton transfer and gas channels that connect the active site to the surface of the enzyme.

There has been significant expansion in the past decade in efforts to design artificial metalloenzymes as structural and functional models of native enzymes.[8–19] Among many different approaches, rational reengineering of existing proteins is an attractive strategy that tests our ultimate understanding of the metallobiochemistry.[20–21] In this approach, typically an existing protein scaffold that does not possess the same function of the target enzyme, is intuitively redesigned to harbor the active site of the target metalloenzyme. Although the designed metalloproteins are stripped-down versions of native enzymes, they contain active site features within the protein matrix, provide proper dielectric environment for aqueous chemistry, and allow introduction of secondary and tertiary sphere interactions in an effort to tune the activity. The rational approach allows investigation of the effect of individual design parameters on the properties of the resulting metalloprotein. Water soluble biomolecular catalysts for hydrogen evolution have been reported in recent years employing peptide appended inorganic components, replacing native heme from hemoproteins with Co-porphyrin (CoP) or synthetic Fe complexes, and by substituting native metal from electron transfer proteins.[22–38]

Herein, we report rational reengineering of an existing copper storage protein (Csp1)[39] into a Ni binding protein (NBP) as a novel ArH featuring a NiS_4 coordination inspired by the [NiFe] hydrogenases. We describe the protein design approaches that led to NBP. NBP binds Ni(II) with proper stoichiometry in a distorted square planar environment with a m icromolar binding affinity. Ni(II)-NBP is a robust and thermostable protein and is active for H^+ reduction to H_2 gas under photochemical and electrochemical conditions. Analysis of the

catalytic voltammograms establish that NBP supports a protoncoupled electron transfer (PCET) mechanism.

RESULTS AND DISCUSSIONS:

A pproaches to redesign C spl into NBP:

In the protein reengineering approach, the selection of a stable protein is critical to incorporate the target active site. We chose the thiol-rich Csp1 from *Methylosinus trichosporium* OB3b (PDB 5FJE), as a scaffold to incorporate the putative Ni site.[40] Csp1 stores and supplies Cu(I) to particulate methane monooxygenase (pMMO) during methane oxidation. Csp1 is a tetramer of four-helix bundles, with each monomer being 122 residues in length (Figure S1a). The first helix comprised of 46 residues is the longest. 13 Cys residues are lined along the central helical core which bind a total of 13 equivalents of Cu(I) (Figure S1b) with very high affinity ($Kd \sim 10^{-18}$M). Ten of the 13 Cu(I) are bound as linear 2-coordinate, while 3 Cu(I) feature 3-coordinate μ_3-S ligation. Among these, Cu4 is bound as tris-thiolato ligation in the center of the bundle, while the Cu11 and Cu13 are recruited at the exposed end. We chose Cu4 (Figure S1c) as a potential location to introduce the NiS_4 site. Cu4 is bound to Cys26, Cys62, and Cys87 at 2.19Å, 2.32 Å and 2.30Å, respectively. A fourth Cys, Cys113 is located 3.71Å away from Cu4 and is involved in bridged ligation to two other Cu(I), Cu1 and Cu3 (Figure S1c). Since Cys residues are known to possess alternate conformations in the absence of metal ions,[41] which can reorient to a different conformation upon metal binding, we hypothesized that in the absence of competing ligation to Cu1 and Cu3, Cys113 may reorient towards Cu4. A PyMol model (Figure S1d) supported this notion that an alternate conformation of Cys113 would bring this residue within bonding distance from Cu4. We therefore, chose to maintain the Cys26, Cys62, Cys87 and Cys113, i.e. one Cys from each of the four helices to form the desired Ni site of NBP. The remaining 9 Cys residues were mutated to 7 Ala, 1 Leu and 1 Val (Figure 2a). The 7 Ala residues were chosen due to the similarity of Ala in size with Cys (Cys33, Cys37, Cys51, Cys90, Cys106, Cys110, and Cys117) so as to maintain a compact helical structure of the target construct. Two bulky hydrophobic residues Val (Cys94) and Leu (Cys103) were introduced towards one of the exposed ends of the protein to provide hydrophobic packing so that the target protein remains well folded. Finally, to avoid competition for Ni binding, all 6 of the His residues were mutated to polar but non-coordinating Asn and Gln residues, 3 each (Figure 2b). Therefore, a total of 15 mutations were introduced in Csp1 to design the NBP (Figure S2).

Computer model of NBP validates the design:

To probe whether these mutations will be tolerated in the design, we generated a computer model of NBP using the NAMD molecular modeling suite.[42] The above 15 mutations were introduced into the crystal structure of apo Csp1 (PDB: 5FJD).[43] An approximately constant RMSD of 1.4–1.6Å was obtained at the end of equilibration, suggesting that the starting model relaxed to a stable structure (Figure 2c). An overlay of the NAMD minimized structure of apo NBP (Figure 2d green) with the crystal structures of apo Csp1 (Figure 2d purple), and Cu(I)-Csp1 (Figure 2d cyan) suggests that the overall secondary and tertiary structures of Csp1 will be retained in the designed NBP. An overlay of the Cys site of apo

Csp1, Cu(I)-Csp1 and the NBP model suggests quite similar overall structures with some variability in Cys26 and Cys62 side chain orientations of Cu(I)-Csp1 as dictated by metal binding, compared to the two apo proteins (Figure S1e). A view of the Cys site perpendicular to the helical axis keeping the N-terminus at the top (Figure 2e), shows the relative orientation of the sulfhydryl groups with respect to the alpha carbon (CA) differ from each other. For Cys26, the beta methylene carbon (CB) and the thiol group (SG) point opposite to each other (up/down). In Cys62 and Cys113, the CB and SG groups point below the CA (down/down), while for Cys87, both the CB and SG groups point above (up/up) the CA carbon. These differences in the Cys orientations indicate asymmetry in the metal binding site of NBP. Similarly, a view of the binding pocket along the helical axis keeping the N-terminus at the top (Figure 2f) shows a thiol-rich pocket suitable to bind metals.

Folding and stability of NBP:

Apo NBP was purified to homogeneity at ~15 mg/L yield (Figure S3), and its identity was verified by MALDI MS (Figure S4; observed = 13520 Da, calculated = 13519 Da). Under native conditions, both apo and Ni(II)-NBP exist as a tetramer (Figure S3) of four helix bundles, similar to Csp1. CD spectrum of apo NBP at pH 8.5 exhibits classical double dips at 222 nm and 208 nm (Figure 3a blue), characteristic of a-helical secondary structure. The apo NBP was found to be in 42% α-helical form (Table 1), similar to 48% α-helical character found for reduced apo Csp1 (Figure 3a black) under similar conditions. In the presence of 1 equivalent Ni(II) both minima of apo NBP became more negative resulting in an increase in the α-helical character to 53% (Figure 3a red) indicative of Ni(II) binding to NBP. Thermal melting experiments showed a steeper transition and accordingly, a higher enthalpy change of unfolding for NBP (ΔH^{unfold} =110 kcal/mol for apo NBP, Figure 3b blue; and 100 kcal/mol for Ni(II)-NBP, Figure 3b red) compared to apo Csp1 (82 kcal/mol, Figure 3b black). These results suggest a higher degree of cooperative unfolding behavior of NBP compared to Csp1, likely attributable to the replacement of the Cys residues in Csp1 with the hydrophobic and helix-inducing residues that we introduced in the NBP design. An approximately 2-fold higher positive ΔCp^{unfold} in apo and Ni(II)-NBP compared to apo Csp1 also suggests a high degree of cooperativity and apolar solvation upon NBP unfolding, attributable to native-like behavior of well folded proteins demonstrating hydrophobic effect. When a melting experiment was performed with apo NBP in the presence of TCEP, a similar melting profile was obtained (Figure S5), indicating that the pre-reduced protein remains reduced during thermal melting (Figure 3). The similar melting profile of apo NBP and the T_m values of apo and Ni(II)-NBP suggest that Ni(II) has little influence on the thermal stability of apo NBP. We hypothesize the inherently high core stability of NBP is not further augmented by Ni(II) coordination, which results in the similar thermal stability of apo and metal-bound NBP. It should be noted that Cu(I) binding to Csp1 did not cause any changes in the helicity, suggestive of high backbone stability of the protein.[39] A higher T_m (73°C) of Csp1 compared to NBP indicate that Csp1 is more thermostable. Nonetheless, a T_m of 58°C for NBP at pH 8.5 suggests that NBP is a well-folded and stable protein.

Ni(II) binds NBP in a distorted square planar geometry and form s a diam agnetic complex:

Electronic absorption spectroscopy.—The UV-vis spectrum of Ni(II)-NBP at pH 8.5 (Figure 4a–b) is characterized by a high energy band at 256 nm (4.84 eV) with $\Delta\varepsilon_{256}$ of

17,740 $M^{-1}cm^{-1}$ (Table 2), which is best assigned as a ligand-to-metal charge transfer (LMCT) transition. Another shoulder band in the UV region is observed at 327 nm (3.79 eV) with $\Delta\varepsilon_{327}$ of 420 $M^{-1}cm^{-1}$. The visible region is represented by a major band at 420 nm (2.95 eV), with $\Delta\varepsilon_{420}$ of 400 $M^{-1}cm^{-1}$, and another low energy feature at 566 nm (2.19 eV) with $\Delta\varepsilon_{566}$ of 87 $M^{-1}cm^{-1}$ characteristic of a d-d transition. From Ni(II) binding titration to apo NBP (Figure S6), a stoichiometry of Ni(II) to protein was found to be ~1.2, suggesting that 1 equivalent of Ni(II) binds to NBP with a Kd41 of ~10 μM. The UV-vis spectrum of NiSO4 in solution is blue shifted compared to the major band in the visible region for Ni(II)-NBP, confirming that the observed spectral features are arising from Ni(II) bound to the protein. Soft thiolate ligands of NBP and differences in geometry could cause the Ni(II) centered transitions move to lower energy compared to hexa-aqua Ni(II). As a control, we expressed and purified a Cys-free variant of NBP (see Materials and Methods), which upon Ni(II) addition was colorless as opposed to the light yellow color observed for Ni(II)-NBP (Figure S7). This result shows that the observed spectral features of Ni(II)-NBP are indeed attributable to Ni-thiolate interactions at the designed metal site. The spectral features of Ni(II)-NBP are reminiscent of square planar, mononuclear, and diamagnetic aryl thiolate complexes of Ni such as $(Et_4N)_2[Ni\text{-}(S\text{-}p\text{-}C_6H_4Cl)_4]$ reported by Maroney and co-workers.[44] In particular, these spectral features and the extinction coefficients argue against a T_d Ni(II) thiolate site such as that of Ni(II)-rubredoxin where intense bands in the visible region with higher extinction coefficients are observed as governed by the T_d symmetry.[45]

X-ray absorption spectroscopy.—We employed nickel K-edge X-ray absorption spectroscopy to directly probe the electronic and geometric structure of Ni(II)-NBP. X-ray absorption near-edge spectroscopy (XANES) was used to probe the coordination number, metal ion geometry and oxidation state. The XANES data for the metalloprotein shown in Figure 5a shows a weak 1s-to-3d pre-edge peak at 8333.4 eV, as well as a poorly resolved shoulder feature centered at 8337.5 eV presumably corresponding to a 1s-to-4p+shakedown transition. The positions of these peaks are consistent with a Ni(II) center in NBP. The combination of spectral features observed here is generally seen in either four-coordinate distorted Ni(II) sites intermediate between square planar and tetrahedral symmetry or in five-coordinate square-pyramidal Ni(II) centers. Notably, Ni(II) sites in T_d, O_h, or trigonal bipyramidal symmetries all lack the higher-energy shoulder feature, while the presence of a 1s-to-3d preedge peak argues against a highly centrosymmetric square planar Ni(II) site.[46]

We then analyzed the extended X-ray absorption fine structure (EXAFS) for the first coordination sphere to uncover details of Ni(II) ligation including identity of the scatterers and metal-ligand bond distances (Table S1). The EXAFS data (Figure 5b) showed a single dominant oscillation pattern giving rise to a peak in the Fourier Transform (FT) with a phase-shifted distance of ~1.7 Å. The best fit consists of a split first coordination sphere of Ni(II) with two Ni-S scatterers at 2.20 Å and two more Ni-S scatterers at 2.37 Å. The EXAFS from both the Ni-S vectors are out of phase with each other leading to destructive interference suppressing the apparent EXAFS signal (Figure S8). This distorted four-coordinate site is consistent with the symmetry inferred from XANES studies. Notably, fits to a single shell of sulfur ligands give significantly worse fit qualities and indefensibly large ΔE_0 values, indicative of a model that does not adequately describe the experimental data.

Likewise, while fits to a nitrogen-dominated first-shell model gave the better fit quality statistics, the bond length and coordination number combination corresponded to a bond valence sum of approximately 1, and are not supported by either the optimized structure or the electronic absorption data. The experimentally derived Ni-S distances from the EXAFS data are in also excellent agreement with the calculated Ni-S bond distances (*videinfra*). The EXAFS data and the optimized structure support our hypothesis in the NBP design that a $NiCys_4$ coordination environment can be accommodated within the protein pocket of Csp1. Together, these data validate the approach to reengineer Csp1 into NBP. To compare, the Ni-S distances in the X-ray structures of [NiFe] hydrogenases range from ~2.2–2.6 Å.[6, 47] EXAFS of various classes of [NiFe] hydrogenases also indicate average Ni-S distances of 2.2–2.4 Å.[48]

1H NMR spectroscopy: We probed the spin state of Ni(II) in NBP by ^{1}H NMR spectroscopy. The NM R spectrum of apo NBP showed well-dispersed peaks in both the aromatic and aliphatic regions (Figure 6 black). In the Ni(II)-bound form of NBP all the peaks overlapped with those of apo NBP with minor broadening of some peaks. However, no hyperfine-shifted resonances (Figure 6 red) was observed in the Ni(II) bound form. This data confirms the presence of planar Ni(II) coordination within NBP with a diamagnetic ground state, corroborating with the XAS data. The NM R spectra of square planar aryl thiolate Ni complexes also form diamagnetic ground state and do not show any shifts in ^{1}H resonances.[44] In contrast, the T_d Ni(II)-rubredoxin complex reported by Moura and co-workers showed paramagnetically shifted resonances,[45] as expected for a triplet ground state of Ni(II).

Structure optimization: The Q M/M M calculations with both $S=0$ and $S=1$ spin states and both square planar (SP) and tetrahedral (TH) coordination geometries were performed to reveal the most favorable active site structure in the presence of protein environment. The singlet NBP can be optimized with both square planar and tetrahedral Ni coordination geometries, see ^{1}NBP-SP and ^{1}NBP-TH in Figure 7a and 7b, respectively. Compared to the active site square planar model of ^{1}Ni-4Cys, the ^{1}NBP-SP is distorted as indicated by a deviation of 16.0° from standard square planar ∠S1-S2-S3-S4 (see Table S2), due to protein environment restraint. For a similar reason, ^{1}NBP-TH also deviates from a standard tetrahedral geometry by ∠S1-S2-S3-S4 of 30.5°, which is more significant than in ^{1}NBP-SP and thus makes ^{1}NBP-TH more unfavorable. Consequently, ^{1}NBP-TH is of higher energy by ΔG of 35.34 kcal/mol based on the QM/MM calculations. In the case of triplet protein calculations, only tetrahedral coordination is stable after QM/MM geometry optimizations, see the QM region structure of ^{3}NBP-TH (Figure 7c). Initialization with a square planar geometry still produced a final tetrahedral coordination after QM/MM geometry optimization. In ^{3}NBP-TH, ∠S1–S2–S3–S4 of 54.7° indicates ~15° smaller distortions from the standard tetrahedral coordination than in ^{1}NBP-TH. The ^{3}NBP-TH model is also of lower energy than ^{1}NBP-TH. Overall, as shown in Table S2, these protein level calculations show that the most favorable structure has singlet Ni with a distorted square planar coordination, which is consistent with experimental work here. In addition, the average Ni-Cys bond length (R_{Ni-S}) of 2.31 Å in ^{1}NBP-SP is in excellent agreement with the experimental average value of 2.29 Å, and has much better agreement with experiment than

the average Ni-Cys bond lengths of 2.35 and 2.44 Å for ^{1}NBP-TH and ^{3}NBP-TH, respectively. Additional computational results in Supporting Information (Figure S9) suggest that the protein environment plays a significant role in determining the final electronic and geometric structure for Ni center here, and the full protein QM/MM calculations are needed to reproduce experimental protein results as reported recently.[49]

Photo-induced H^+ reduction by NBP:

We next tested whether Ni(II)-NBP can generate H_2 gas under photochemical conditions employing $Ru(bpy)_3^{2+}$ as a photosensitizer and ascorbate as a sacrificial electron donor. Solutions containing 2 μM protein were irradiated using a white light source and the head space gas was analyzed by GC (Figure S10). Presence of H_2 gas in the head space was detected within 30 min of irradiation. The H_2 production saturated within 2 h with a turn over number (TON) of ~ 115 (Figure 8 blue), corresponding to a turn over frequency (TOF) of ~1/min.

This TOF is at par with the CoP substituted myoglobin system, and higher than other biomolecular catalysts.[22–23, 31–32] Significantly less amounts of detectable H_2 were formed in apo NBP (Figure 8 red) and $NiSO_4$ (Figure 8 black) under similar experimental conditions. In the absence of $Ru(bpy)_3^{2+}$, no H_2 was formed (Figure 8 green) in Ni(II)-NBP. These results, therefore, suggest that the Ni(II)-NBP is a catalyst under photochemical conditions, and that it is an ArH. We probed the mechanism of H_2 production by Ni(II)-NBP by examining the possibility of a reductive quenching pathway. Previous studies have shown that photoexcited $*Ru(bpy)_3^{2+}$ is quenched by ascorbic acid and produces $Ru(bpy)_3^{1+}$, which subsequently reduces the catalyst.[50–51] To test this possibility under our experimental conditions, we monitored the fluorescence emission of $Ru(bpy)_3^{2+}$ as a function of ascorbic acid concentration (Figure S11). A gradual decrease in the emission intensity of $Ru(bpy)_3^{2+}$ was observed where the photoexcited state decayed following a Stern-Volmer relationship with a quenching rate constant of 2.18×10^7 $M^{-1}s^{-1}$ under our conditions. Since molecular catalysts[52–53] have been shown to directly quench $*Ru(bpy)_3^{2+}$ we also examined whether Ni(II)-NBP is capable of the same. Figure S11c demonstrates that Ni(II)-NBP does not directly quench $*Ru(bpy)_3^{2+}$. Therefore, the best mechanistic model that describes the observed catalysis data is that $Ru(bpy)_3^{1+}$ produced by ascorbate quenching acts as the reducing agent to reduce Ni(II)-NBP into the catalytically active form leading to H_2 generation. The large negative redox potential of $Ru(bpy)_3^{1+}$ (−1.23 V vs NHE)[54] makes it thermodynamically capable of reducing Ni(II)-NBP into its active form.

Electrochem ical studies of NBP:

Voltammetry: Having probed the photochemical behavior of Ni(II)-NBP, we next investigated the pH-dependent catalytic H^+ reduction activity of this metalloprotein using protein film electrochemistry (PFE).[55–58] For these experiments 10 μL of 170 μM proteins were drop-cast on a pyrolytic graphite electrode (PGE), dried under a gentle stream of N_2 gas and voltammograms were recorded in N_2-saturated mixed buffer solutions at varying pH values (Figures 9a, S12). With a decrease in pH, a sharp catalytic peak in the voltammograms was observed (Figure 9a) in the pH range 4–6. The apparent potentials for the fall of the catalytic wave cathodically shifted with an increase in pH, indicating that the

catalytic process is pH dependent. In contrast to Ni(II)-NBP, apo NBP showed no activity indicating the observed activity required Ni. No redox peak corresponding to a Ni^{II}/Ni^{I} process was observed in the voltammograms of adsorbed protein in the studied pH range. In PFE studies of native and artificial hydrogenases the redox ET peaks are also not commonly observed.[22, 59–60] The lack of appearance of a Ni^{II}/Ni^{I} redox couple suggests that the electron transfer, H^+ transfer and chemical steps all occur concurrently within the catalytic wave. The observed potentials corresponding to a current density of −1 μA/cm^2 obtained from the averages of the cathodic and anodic waves (Figure S13) suggested that in the pH range 4–7 Ni(II)-NBP operates at an η of ~560–510 mV measured as the difference between the observed potentials at these current densities ($E_{i=-1\mu A/cm2}$) and the thermodynamic potential for H_2 production at the respective pH values. Although these values of η are higher than native [NiFe] hydrogenases, we note that these overpotentials are lower than or similar to biomolecular and molecular catalysts.[22–23, 25, 27, 3363] A Pourbaix diagram (Figure 9b) demonstrates a linear relationship between the redox potentials $E_{i=-1\mu A/cm2}$ and pH with a slope of 55 mV/pH, suggesting that Ni(II)-NBP catalysis can be described by a proton-coupled electron transfer (PCET) mechanism.[22, 59–60] The redox potential for the catalytic wave in alkaline condition (E^{alk})[59–62] was derived to be −0.95 V vs NHE with an acidity constant (pK_a) of ~7.3 from the analysis of the Pourbaix diagram.

Controlledpotential electrolysis (CPE) confirms H_2 evolution.—We next employed CPE under inert atmosphere to test the efficiency of H_2 production using 7 mL of 25 μM protein solutions polarized at −1V vs NHE for 1h at pH 5 (Figures 9c–d, S14–S16) using a graphite rod electrode (see Materials and Methods). The total charge passed during the experiment was 4.7 C for Ni(II)-NBP (Figure 9c blue) corresponding to a TON of ~210 (Figure 9d). To probe into the true nature of the catalyst, we performed the rinse test of the electrode after electrolysis by gently washing the electrode followed by re-immersing the electrode in degassed blank buffer and re-polarizing the electrode for 1 h of electrolysis. A negligible amount of charge (Figure 9c orange) passed producing background level H_2 (Figure 9d). This data indicates the homogeneous nature of the Ni(II)-NBP catalyst, as opposed to deposited heterogeneous Ni particles. The TON from CPE of Ni(II)-NBP at pH 6 was obtained to be ~110 (Figure S15), which qualitatively correlated with the relative catalytic currents in the voltammograms at pH 5 and 6. Separate control CPE experiments with blank buffer produced an insignificant amount of charge (Figure 9c gray), while in apo NBP (Figure 9c red) and NiSO4 (Figure 9c black) samples ~0.2 C, and ~1 C charge was passed under similar conditions (pH 5) producing small amounts of H 2. These results demonstrate the catalytic nature of Ni(II)-NBP compared to control samples. From calculation of the total number of electrons consumed with respect to the total charge passed during CPE, a near quantitative Faradaic efficiency (FE) of 93±5% was obtained for Ni(II)-NBP, while for apo NBP, $NiSO_4$ and blank buffer the corresponding FE were 52%, 32%, and 12%, respectively (Table S3). These results demonstrate that although ~1C charge passed in the CPE of $NiSO_4$ only 32% contributed to H_2 production. The high FE is similar to the biomolecular Co cata-lysts,[25, 27, 33, 64] and many molecular catalysts,[63,65] but significantly higher than other reported systems.[22] To probe into the UV-Vis spectral changes of Ni(II)-NBP after electrolysis (Figure S16) we collected CD and MALDI-MS data of the samples before and after electrolysis. As can be seen in Figure S17, the ratios of $\theta 222/\theta 208$ became

less than 1 at both pH 5 and 6 (0.98 Figure S17a green and 0.93 in Figure S17b green) after electrolysis, compared to the corresponding samples before electrolysis where $\theta 222/\theta 208$ values were 1.1 (Figure S17a red) and 1 (Figure S17b red), respectively. These results indicate minor changes in the helix orientations upon electrolysis. The MALDI-MS data showed an intact mass of the protein without any fragmentation (Figure S17 c,d) after electrolysis. It is plausible that small alterations in helix orientations imparts changes in the coordination environment and geometry around the Ni site that can lead to the observed differences in the optical spectra. Further studies would be required to fully understand the salient structural and electronic changes that lead to the observed differences in the UV-Vis spectra before and after electrolysis.

CONCLUSIONS:

In conclusion, here we have described the rational design of a novel ArH metalloprotein by reengineering a copper storage protein whose native function is to store and supply Cu(I) to pMMO, as opposed to hydrogen evolution. A hypothesis driven intuitive design process involved removing all but one of the Cu(I) sites in the central location of the four helix protein followed by repacking the hydrophobic core and replacing competitive metal ligands. This strategy led to the creation of a tetrathiolate Ni(II) binding protein (NBP) that is well folded and stable in solution showing native-like unfolding behavior. Electronic absorption, XAS, NM R and QM/MM studies revealed that a distorted square planar diamagnetic NiS4 coordination is formed within NBP. The QM/MM studies also revealed that the protein matrix preferentially stabilizes the singlet distorted square planar coordination over the triplet tetrahedral coordination. Together, these data corroborated the design approach. When deposited as films on PGE, Ni(II)-NBP displayed pH-dependent catalytic H^+ reduction with η of ~560–510 mV that is comparable to other biomolecular and molecular catalysts. Analysis of the catalyti c voltammograms indicated a PCET mechanism. Electrolysis confirmed the evolution of H_2 with a TON of ~210 after 1 h with near quantitative FE. Spectroscopic studies suggested small changes in the protein secondary structure after electrolysis. Ni(II)-NBP follows a reductive quenching mechanism, producing H_2 under photochemical conditions with a TOF of ~1/min, which is comparable to or higher than reported biomolecular catalysts. In summary, this study demonstrates the successful implementation of rational metalloprotein design approach into creating an ArH.

MATERIALS AND METHODS:

General procedures:

All reagents were used as received without further purification. All the glassware and plasticware used for the experiments were soaked in 10 mM ethylenediaminetet-raacetic acid (EDTA from VWR) bath overnight, followed by overnight soaking in 10%, and 1% nitric acid baths, respectively. These were then thoroughly washed with deionized water. All buffers were Chelexed (Sigma Aldrich) overnight followed by pH adjustment and filtration.

NAMD modeling:

NAMD modeling was performed using unmodified CHARMM22 force field included in the parameter file “par_all27_prot_lipid.prm” employing resources at the Mississippi Center for Supercomputing Research (MCSR). Starting with the X-ray structure of apo Csp1 (PDB: 5FJD), all the 15 mutations were introduced followed by addition of hydrogens in NAMD. The structure was hydrated within a box of 66Å ×52Å ×66Å and ionized with 0.5M KCl, followed by minimization for 5000 steps and equilibration time of 1 ns.

Protein expression and purification:

A synthetic gene of NBP (see the SI) with an N-terminal Strep-tag (WSHPQFEK) followed by a GGS spacer was cloned (Genscript) into pET 29a (+) vector at the NdeI/NcoI restriction sites. The gene was dissolved at 100 ng/μL in Milli-Q water and stored at −20 °C. To 1 μL of NBP gene in a 10 mL culture tube pre-cooled on ice, 50 μL of *E.cloni* EXPRESS DUOs BL21(DE3) chemically competent cells (Lucigen) were added and incubated in ice for 30 min. The cells were then subjected to heat shock at 42 °C for 45 s and further incubated in ice for an additional 10 min. Cells were recovered with 1 mL of LB media in an incubator-shaker (Thermo Fisher MAXQ 4000) at 37 °C for 1 h. 50 μL of the cells were then plated on kanamycin LB agar plates and incubated at 37°C overnight. 10 mL primary cultures in LB media supplemented with 50 mg/mL kanamycin (Fisher) were inoculated with single colonies and grown overnight at 180 rpm at 37 °C. 1 L of secondary cultures in LB media supplemented with kanamycin were inoculated with 10 mL of primary cultures and grown for 3–4 h at 180 rpm, 37 °C, until the OD600 reached ~0.55. At this point, the cultures were induced with 1 mM (final concentration) of Isopropyl β-D-1-thiogalactopyranoside (IPTG from Goldbio). The induced culture was then allowed to grow for 6 h, at 180 rpm at 30 °C. 10 mL of un-induced culture was grown, pelleted and sonicated under the conditions similar to that of the induced culture and then checked as a control on the gel. The cells were harvested at 6000 rpm (SORVALL RC 5B PLUS) for 10 min and the pellets were stored in −20 °C overnight. Next day, the pellets were re-suspended in 50 mL of lysis buffer consisting of 20 m M tris(hydroxymethyl)aminomethane (Tris.HCl from VWR) pH 8.5, 1 mM dithiothreitol (DTT from VWR), 1mM phenylmethane sulfonyl fluoride (PMSF from Biosynth Inc.), 1 mM EDTA and 10 μg/mL deoxyribonuclease (DNase I from Worthington Biochemical Corp.), followed by sonication on ice (Branson) for 3 min using a 10 s on, 20 s off cycle. The lysate was then centrifuged in SS–34 rotor (Thermo Fisher SORVALL RC6 + Centrifuge) at 14000 rpm for 45 min at 4 °C. The supernatant was then filtered through a 0.45 μm filter and used for purification using Strep-Tactin affinity columns (GE Healthcare) pre-equilibrated with wash buffer (100 mM Tris, 150 mM NaCl, 1 mM EDTA, pH 8.0). The supernatant was loaded onto a 5 mL column at 4 mL/min flow rate using an Econo gradient pump (Bio-Rad) followed by washing with 5 column volumes (20 mL) of wash buffer to remove unbound proteins. The protein was eluted using 20 ml of elution buffer consisting of 100 mM Tris-HCl, 150 mM NaCl, 1 mM EDTA, pH 8.0, 2.5 mM D-desthiobiotin (Sigma Aldrich). The columns were regenerated using 10 mL water followed by 16 ml of 0.5 M NaOH. The columns were then washed with 20 mL water to remove the NaOH. Once the pH was neutral, the columns were stored back in the wash buffer. Following the affinity purification step, the protein was further purified by size exclusion chromatography. The protein was concentrated to 2 mL using 10 kDa MWCO

filters (Millipore), centrifuging at 4000 rpm (Thermo Fisher Heraeus Megafuge 16R) for 5 min and filtered using 0.22 μM filter (VWR). 1 mM of (tris(2-carboxyethyl)phosphine) (TCEP from Goldbio) was added to the protein and loaded into an SEC column (GE Healthcare XK 16 High Load 16/60, Superdex 75, prep grade) with a 2 ml injection loop. The purification was performed on an AKTA purifier 10 using 50 mM Tris, 150 mM NaCl pH 7.8 as the elution buffer at a flow rate of 1 mL/min The fraction corresponding to the protein peak (56–63 mL elution volume: Figure S4) was taken and its concentration was determined using ε_{280nm} = 8480 $M^{-1}cm^{-1}$. The purified protein was stored at −80 °C. The entire purification cycle of NBP takes five days.

The Cys-free variant of NBP (Cys26Ala/Cys62Val/Cys87Ala/Cys113Val NBP) was expressed and purified to homogeneity according to same procure to that of NBP with a yield of ~13 mg/L of bacterial culture. The purity and mass of the protein was verified by SDS-PAGE and MALDI MS (observed 13516 Da; calc. 13518 Da), respectively (Figure S18a–b). The no-Cys variant was folded in solution as an a-helix (Figure S18c).

Gel electrophoresis:

The induction efficiency and purity of the protein was checked using 12% Tris-Tricine SDS PAGE (12% stacking and 12% resolving gel). 20 μL of each sample was mixed with 5 μL of loading dye (Thermo Fisher) and heated at 90 °C for 10 min. 15 μL of each analyte was then loaded onto the gel and run at 100 V for 3 h in a water circulated electrophoresis chamber (Thermo Fisher). Native gel was performed using a 10% stacking, 12% resolving gel in the presence of 5% 2-mecapto ethanol (Fisher) without the SDS and heat treatment. The gels were stained in 0.3% coomassie blue solution in 45% Methanol, 10% glacial acetic acid, 45%, H_2O and de-stained in 30% methanol, 10% glacial acetic acid, 60% H_2O mixture.

MALDI-MS-

MALDI-MS was used to determine molecular weight of the protein. 1 μL of 50:50 NBP:sinapinic acid matrix (Sigma Aldrich: 10 mg/mL in 50:50 acetonitrile:water with 0.1% TFA) mixture was spotted on a 100-SS plate (JBI Scientific) and analyzed using an Applied Biosystems Voyager-DE instrument. The lowest possible laser threshold was used to ionize the protein.

Thiol quantification:

Thiol quantification of NBP was performed using Ellman's reagent 5,5′-dithiobis-(2-nitrobenzoic acid) (DTNB, Acros Organics) under two different conditions: i) without guanine hydrochloride (GuHCl) and ii) with GuHCl (VWR). The samples for i) contained 1 M Tris pH 8, water, 2 mM DTNB in 50 mM sodium acetate (Alfa Aesar), and NBP at a ratio (v/v) of 10%, 77%, 5%, and 8 %, respectively. Samples for ii) were similar to i) except that 6 M GuHCl pH 8.5 was used instead of water. The samples in triplicate were incubated for 15 min prior to quantification using ε_{412nm} = 14,150 $M^{-1}cm^{-1}$.[39, 66] Without added GuHCl, almost no reaction of DTNB occurred with the Cys thiols, consistent with a compact structure of NBP and similar to what was observed for apo Csp1 as well.[39] The DTNB assays indicated ~15% of Cys was oxidized. Subsequent reduction of NBP with 4-fold excess of TCEP followed by two PD10 columns to remove excess TCEP recovered 100% of

the sulfhydryl groups. Therefore, all subsequent metallation studies were performed by reduction of apo NBP with TCEP followed by removal of the excess reducing agent.

Circular dichroism spectroscopy:

Frozen stocks of NBP were thawed and reduced with 4 equivalents of TCEP. After 15 min of incubation, the protein was exchanged into 5 mM Tris buffer pH 8.5 using a PD10 column (GE Healthcare). CD scans were collected on an AVIV spectrometer under constant flow of N_2 using 3.5 μM proteins. The melting experiments of apo and Ni(II)-NBP were performed by monitoring the CD signal at 222 nm in the temperature range of 15 °C-95 °C.

Analysis of CD m elting curves:

Analysis of the thermal melts were performed using Gibbs-Helmholtz equation assuming a two-state folded $\rightleftharpoons$ unfolded model with temperature independent ΔH^{unfold} and $\Delta C_p{}^{unfold}$.[67] The following variables and parameters were used;

variables:

i) baseline for native state:

$$B = N + L * (x+273) \quad \text{i}$$

where N is the CD signal (θ_{222}) for native state, L is the slope of the native baseline, x is the measured temperature in °C

ii) baseline for unfolded state:

$$D = U + P * (x+273) \quad \text{ii}$$

where U is the CD signal (θ_{222}) for unfolded state, P is the slope of the unfolded baseline, x is the measured temperature in °C

iii) span between the folded and unfolded baselines:

$$A = B - D \quad \text{iii}$$

iv) folding constant at each temperature:

$$K = \exp\left(-\frac{H * \left(1 - \frac{x+273}{M+273}\right) + C * \left(x - M - (x+273) * \ln\left(\frac{x+273}{M+273}\right)\right)}{R * (x+273)}\right) \quad \text{iv}$$

where H = ΔH^{unfold} in kcal/mole

M = melting temperature in °C

C = ΔC_p^{unfold} in kcal/mole/K

R = universal gas constant in kcal/mole/K = 0.0019872

v) fit

$$Y = A * (K/1 + K) + D \quad \text{v}$$

equations i, ii, iii, and v were formulated in Origin and the plot of θ_{222} vs t (in °C) was fit.

Ni(II) titration m onitored by UV-vis:

Ni(II) titration to apo NBP was performed by anaerobic addition of $NiSO_4$ to reduced apo NBP at 50 μM concentration in 50 mM Tris pH 8.5, and spectral changes were monitored using a Cary 5000 UV-vis NIR spectrophotometer (Agilent). Stocks of apo NBP were reduced with ~4-fold excess TCEP, purified by PD10, concentrated, and loaded into degassed anaerobic cuvettes (Starna Cells). Ni(II) was added at 0.2 equivalent increments using a gas-tight syringe (Hamilton) kept inside a degassed Schlenk flask. Enough time (15 min) was allowed to reach equilibrium after each Ni(II) addition prior to data collection. The absorbance of apo NBP was subtracted from the Ni(II)-bound spectra to obtain the differential absorbance. The differential absorbance (ΔA) at 256 nm was plotted as a function of equivalents of Ni(II) and the binding curve was analyzed to obtain the K_d of Ni(II) binding to NBP.[41]

Preparation of Ni(II)-NBP:

Apo NBP was reduced with 4-fold excess TCEP and purified using PD 10 columns pre-equili-brated in 20 mM Tris buffer pH 8.5. The concentration of the protein was determined using an Agilent 8454 diode array UV-vis spectrometer. Ni(II)-NBP was prepared at room temperature by addition of 1 equivalent of $NiSO_4$ to apo NBP under anaerobic conditions, added at 0.25 equivalent each time at an interval of 10 min under constant stirring. The protein was stored at 4 °C overnight with continuous stirring. The Ni(II)-NBP was then purified by either PD10 or 10 kDa MWCO filters to remove any unbound metal. Whenever necessary, the Ni(II)-NBP was concentrated using 10 kDa MWCO filters as well. The binding of Nickel was confirmed using UV-vis spectroscopy.

X-Ray absorption spectroscopy:

Ni(II)-NBP samples for XAS were prepared at 1.5 mM final concentration using the same procedure as described above. Concentrated samples of the protein were mixed with glycerol as a glassing agent to a 2 0 % final concentration, loaded into sample cells which were sealed with Kapton tape and flash frozen in liquid nitrogen. XAS data was measured on beamline 7–3 at the Stanford Synchrotron Radiation Lightsource (SLAC National Accelerator Laboratory, Menlo Park, CA, USA), with the storage ring operating at 3.0 GeV and 500 mA. A liquid-nitrogen cooled Si(220), φ = 0° double crystal monochromator was used for monochromatic energy selection, and was detuned 50% 1000 eV above the Ni K-edge for harmonic rejection. Sample temperatures were maintained at 15K using a closed-

cycle liquid He cryostat. XAS spectra were collected in a fluorescence geometry with a 30-element germanium detector (Mirion), using the following scan parameters: 10 eV steps/1 sec. integration time in the pre-edge, 0.3 eV/2 sec. integration times for the edge region, and 0.05k steps in the EXAFS region, with integration time increasing in a k^2-w eighted fashion from 2 to 10 sec over the energy range (k_{max} = 16.1k). Total detector counts/element were kept below 30k, using a Soller slit assembly and 6μ cobalt oxide filter to reduce scatter. A Ni metal foil spectrum was collected simultaneously for energy calibration, with the first inflection point set to 8333.0 eV. Data was collected on 5 distinct spots, as multiple scans on a given spot showed evidence of radiation damage based on changes in the shape and intensity of edge features. Only the first scan at each spot was considered for data analysis.

Averaging and normalization of the XAS data was carried out using Athena, while Artemis was employed for EXAFS analysis.[68] A simple first-shell scattering model was constructed and used as FEFF input to obtain phase and amplitude parameters for Ni-N, Ni-O, and Ni-S scatterers at various distances. For a given shell in all simulations, the coordination number n was fixed, while r and a 2 were allowed to float. The amplitude reduction factor S_0^2 was fixed at 0.9, while the edge shift parameter ΔE_0 was allowed to float at a single common value for all shells. The fit was evaluated in k^3-weighted R-space, and fit quality was judged by the reported R-factor. Significant fits are tabulated in Table S1.

^{1}H NMR spectroscopy:

NMR data were collected at RT in a Bruker 500 MHz spectrometer equipped with a 5 mm broadband cryo probe employing a watergate pulse program for water suppression with a relaxation delay of 2 ms. For each sample 1024 scans were collected. Samples contained 400 |±M of apo or Ni(II)-NBP in 0.1 M phosphate buffer pH 8.1 with 0.1 M NaCl prepared in 10% D_2O. Data processing was performed in MestReNova.

QM and QM/MM computational details:

Both quantum mechanics (QM) calculations on active site models and hybrid QM and molecular mechanics (MM) calculations on Ni binding proteins (NBPs) were performed. Ni and its four coordinated cysteines 26, 62, 87, and 113 are included in the QM calculations of the active site models, with cysteine being simplified to CH_3CH_2S-, i.e. truncated at the C a position. Geometry optimizations and subsequent frequency calculations were done by using Gaussian 09[69] with the density functional theory (DFT) method B3LYP,[70–71] and the 6–311++G(2d,2p) basis for Ni and four coordinated S atoms, and 6–31G(d) for the remaining atoms. In each case, the frequency analysis was used to verify the nature of the stationary points on respective potential energy surfaces and to provide zero-point energy corrected electronic energies (E_{ZpE}'s), enthalpies (H's), and Gibbs free energies (G's) at room temperature and 1 atm.

For QM/MM calculations, the ONIOM method[72–75] was used. The initial NBP was based on the minimized structure of apo NBP with Ni(II) added and necessary corrections of missing/wrong atoms. The QM region composes of Ni and four coordinated Cys residues, the same as above QM active site model, which was also treated with the same method and basis set as above. The rest part of protein is the MM region, treated using the Amber force

field.[76] The Merz-Singh-Kollman[77] (MK) charges were used for Ni and four coordinated cysteines and Amber charges[76] were used for MM atoms. A few missing AMBER force field parameters were developed in the same way as in the AMBER system.[76] The van der Waals radii and potential well depth results are from the previous study.[78]

Electrochem ical studies:

All electrochemical studies were performed on a Pine Wave Driver 20 bipotentiostat using PGE as the working electrode (Pine), Pt wire (Sigma Aldrich) as the counter electrode and Ag/AgCl (BASi) as the reference electrode. The PFE experiments were performed by dropping 10 μL of 170 μM proteins on PGE, followed by drying under a gentle flow of nitrogen. Data were collected at 15 °C with temperature controlled by a circulated water bath (Thermo Fisher) connected to a multi-necked electrochemical cell. A scan rate of 10 mV/s and an electrode rotation rate of 2000 rpm controlled using an MSR electrode rotator (Pine) were used. All the experiments were performed using a 20 mM mixed buffer solution of sodium acetate, 2-ethanesulfonic acid (MES from Gold Bio), 4- (2-hydroxyethyl)-1-piperazineethanesulfonic acid) (HEPES from VWR), and Tris (VWR) in 0.1 M KCl (VWR) as the supporting electrolyte.

The controlled potential electrolysis (CPE) experiments were performed with 7 mL solutions containing 25 μM proteins in MES buffer under constant stirring in a 50 mL three necked pear shaped flask using a 3 mm graphite rod (Sigma Aldrich) as the working electrode polarized at −1.2 V vs Ag/AgCl. The counter electrode and reference electrode were separated from the main chamber using a fritted tube (ACE glass) and a bridge tube, respectively. For rinse test, the graphite electrode was gently washed with 20 mM Tris buffer pH 8.5 (pI of NBP is 5.1) and water immediately after 1 h CPE experiment of Ni(II)-NBP. The electrode was then placed in the degassed blank buffer at pH 5 and subjected to CPE for 1 h. All CPE experiments were performed under inert atmosphere. To measure H_2 production, 250 μL of headspace gas was syringed out after 1 h of CPE using a Pressure-Lok precision analytical syringe (VICI) stored under N_2 atmosphere, and was detected using a thermal conductivity detector (TCD) connected to a 7890B GC instrument (Agilent) with He as the carrier gas. The area under the curves for the H_2 peaks were converted to ppm using known instrument calibrations. The TON was calculated from the ratio of the moles of H_2 produced to the moles of the catalyst. The UV-vis studies were done immediately before and after the CPE. No H_2 gas was detected when using glassy carbon rod (3 mm diameter, Alfa Aesar) as the working electrode. The experimentally applied potential vs Ag/AgCl was converted to NHE using $E_{nhe} = {}_{EAg/AgCl} + 0.197$.

Ni(II)-NBP samples after electrolysis were dialyzed against 5 mM Tris buffer pH 8.5 to remove excess salts prior to recording CD and MALDI-MS data. The same samples before electrolysis were also dialyzed to ensure similar treatment of all the samples so that direct comparison between the samples before and after electrolysis can be made.

Electrochem ical analysis:

The raw CV data were baseline subtracted using QSOAS software.[79] The Pourbaix diagram was plotted using the $E_{i= -1\mu A/cm2}$ (NHE) from averaged cyclic volt-ammograms at different pH, and fit according to eq. vi.[59–62]

$$E = E^{alk} + 2.303\left(\frac{RT}{nF}\right)log\left[1 + \frac{10^{-pH}}{10^{-pKa}}\right] \quad \text{(vi)}$$

Photo-induced catalysis:

The experiments under photochemical conditions were performed with 2 mL solutions of 2 μM proteins, 1 mM of the photosensitizer Tris (2,2'-bipyridine) dichlororuthenium(II)hexahydrate, $Ru(bpy)_3Cl_2.6\ H_2O$ (Alfa Aesar), 100 mM of sacrificial electron donor ascorbic acid (VWR) in 1 M phosphate buffer at pH 7. The contents were added in a septa-capped pyrex tube and degassed with N_2 gas prior to photo exposure. The phototube was placed at 30 cm distance from a mounted LED neutral white (λ>400 nm; Thor labs) light as the power source was adjusted to 180 mW. The lamp was warmed up for at least 1 h prior to the experiment, and the illuminations were performed for 4 h with a constant stirring at 450 rpm. 250 μL of head space gas was injected and analyzed every 30 min using GC. Efforts to employ other photosensitizers such as erythrosine B and triethanolamine (TEOA) as base for H_2 generation were not successful.

Photolum inescence quenching:

2.5 mL solution of 1 mM $Ru(bpy)_3Cl_2.6\ H_2O$ in 1 M phosphate buffer pH 7 was taken in a fluorescence cuvette of 1 cm path length and the emission spectra (λ_{ex} = 510 nm, λ_{em} = 610 nm) were recorded as a function of ascorbate concentration ranging from 2–58 mM using a PTI fluorimeter. Spectra were recorded after 10 min stirring during each addition. The quenching rate constant (k_q) was obtained from the spectra using Stern Volmer analysis (eq. vii). The ratio of initial intensity to final intensity (F_0/F) was plotted against product of the quencher concentration [Q] and lifetime of fluorophore in the absence of quencher (τ_0 of $Ru(bpy)_3^{2+}$ in water is 0.630 μs) to get the slope (kq).

$$\frac{F_0}{F} = 1 + k_q\tau_0[Q] \quad \text{vii}$$

Similar experiments were also performed using Ni(II)-NBP in lieu of ascorbate by varying the concentration from 1.7 μM to 16 μM. No quenching was observed using Ni(II)-NBP.

Supplementary Material

Refer to Web version on PubMed Central for supplementary material.

ACKNOWLEDGMENTS

Use of SSRL was made possible by support from the U.S. Department of Energy, Office of Science, Office of Basic Energy Sciences under Contract No. DE-AC02-76SF00515. The SSRL Structural Molecular Biology Program is supported by the DOE Office of Biological and Environmental Research, and by the National Institutes of Health, National Institute of General Medical Sciences (including P41GM103393). E.R.F. is supported by NIH P30-EB-009998. Y.Z. is supported by an NIH grant GM085774. S.C. thanks the University of Mississippi, the Oak Ridge Associated Universities for Ralph E. Powe Junior Faculty Award, and the NIH (grant 1R15GM131260-01) for support.

REFERENCES:

1. Armstrong FA; Fontecilla-Camps JC A Natural Choice for Activating Hydrogen. Science 2008, 321, 498–499. [PubMed: 18653870]
2. Fontecilla-Camps JC; Volbeda A; Cavazza C; Nicolet Y Structure/Function Relationships of [NiFe]- and [FeFe]-Hydrogenases. Chem. Rev 2007, 107, 4273–4303. [PubMed: 17850165]
3. Lubitz W; Ogata H; Rudiger O; Reijerse E Hydrogenases. Chem. Rev 2014, 114, 4081–4148. [PubMed: 24655035]
4. Ogata H; Lubitz W; Higuchi Y [NiFe] Hydrogenases: Structural and Spectroscopic Studies of the Reaction Mechanism. Dalton Trans 2009, 7577–7587. [PubMed: 19759926]
5. Ogata H; Lubitz W; Higuchi Y Structure and Function of [NiFe] Hydrogenases. J. Biochem 2016, 160, 251–258. [PubMed: 27493211]
6. Volbeda A; Charon MH; Piras C; Hatchikian EC; Frey M; Fontecilla-Camps JC Crystal Structure of the Nickel-Iron Hydrogenase from *Desulfovibrio gigas*. Nature 1995, 373, 580587.
7. Ogata H; Nishikawa K; Lubitz W Hydrogens Detected by Subatomic Resolution Protein Crystallography in a [NiFe] Hydrogenase. Nature 2015, 520, 571–574. [PubMed: 25624102]
8. Zastrow ML; Peacock Anna FA; Stuckey JA; Pecoraro VL Hydrolytic Catalysis and Structural Stabilization in a Designed Metalloprotein. Nat. Chem 2012, 4, 118–123.
9. Yeung N; Lin Y-W; Gao Y-G; Zhao X; Russell BS; Lei L; Miner KD; Robinson H; Lu Y Rational Design of a Structural and Functional Nitric Oxide Reductase. Nature 2009, 462, 1079–1082. [PubMed: 19940850]
10. Faiella M; Andreozzi C; de Rosales RTM; Pavone V; Maglio O; Nastri F; DeGrado WF; Lombardi A An Artificial Di-Iron Oxo-Protein with Phenol Oxidase Activity. Nat. Chem. Biol 2009, 5, 882–884. [PubMed: 19915535]
11. Rufo CM; Moroz YS; Moroz OV; Stohr J; Smith TA; Hu X; DeGrado WF; Korendovych IV Short Peptides Self-Assemble to Produce Catalytic Amyloids. Nat. Chem 2014, 6, 303–309. [PubMed: 24651196]
12. Solomon LA; Kodali G; Moser CC; Dutton PL Engineering the Assembly of Heme Cofactors in Man-Made Proteins. J. Am. Chem. Soc 2014, 136, 3192–3199. [PubMed: 24495285]
13. Farid TA; Kodali G; Solomon LA; Lichtenstein BR; Sheehan MM; Fry BA; Bialas C; Ennist NM; Siedlecki JA; Zhao Z Elementary Tetrahelical Protein Design for Diverse Oxidoreductase Functions. Nat. Chem. Biol 2013, 9, 826–833. [PubMed: 24121554]
14. Miner KD; Mukherjee A; Gao YG; Null EL; Petrik ID; Zhao X; Yeung N; Robinson H; Lu Y A Designed Functional Metalloenzyme that Reduces O2 to H_2O with Over One Thousand Turnovers. Angew. Chem. Int. Ed 2012, 51, 5589–5592.
15. Song WJ; Tezcan FA A Designed Supramolecular Protein Assembly with in vivo Enzymatic Activity. Science 2014, 346, 1525–1528. [PubMed: 25525249]
16. Tegoni M; Yu F; Bersellini M; Penner-Hahn JE; Pecoraro VL Designing a Functional Type 2 Copper Center that has Nitrite Reductase Activity within a-Helical Coiled Coils. Proc. Natl. Acad. Sci. U.S.A 2012, 109, 21234. [PubMed: 23236170]
17. Mann SI; Heinisch T; Weitz AC; Hendrich MP; Ward TR; Borovik AS Modular Artificial Cupredoxins. J. Am. Chem. Soc 2016, 138, 9073–9076. [PubMed: 27385206]
18. Mathrubootham V; Thomas J; Staples R; McCraken J; Shearer J; Hegg EL Bisamidate and Mixed Amine/Amidate NiN2S2 Complexes as Models for Nickel-Containing Acetyl Coenzyme A

Synthase and Superoxide Dismutase: An Experimental and Computational Study. Inorg. Chem 2010, 49, 5393–5406. [PubMed: 20507077]

19. Neupane KP; Gearty K; Francis A; Shearer J Probing Variable Axial Ligation in Nickel Superoxide Dismutase Utilizing Metallopeptide-Based Models: Insight into the Superoxide Disproportionation Mechanism. J. Am. Chem. Soc 2007, 129, 14605–14618. [PubMed: 17985883]
20. Petrik ID; Liu J; Lu Y Metalloenzyme Design and Engineering Through Strategic Modifications of Native Protein Scaffolds. Curr. Opin. Chem. Biol 2014, 19, 67–75. [PubMed: 24513641]
21. Ward TR Artificial Metalloenzymes Based on the Biotin-Avidin Technology: Enantioselective Catalysis and Beyond. Acc. Chem. Res 2011, 44, 47–57. [PubMed: 20949947]
22. Slater JW; Shafaat HS Nickel-Substituted Rubredoxin as a Minimal Enzyme Model for Hydrogenase. J. Phys. Chem. Lett 2015, 6, 3731–3736. [PubMed: 26722748]
23. Roy A; Madden C; Ghirlanda G Photo-Induced Hydrogen Production in a Helical Peptide Incorporating a [FeFe] Hydrogenase Active Site Mimic. Chem. Commun 2012, 48, 98169818.
24. Sommer DJ; Vaughn MD; Ghirlanda G Protein Secondary-Shell Interactions Enhance the Photoinduced Hydrogen Production of Cobalt Protoporphyrin IX. Chem. Commun 2014, 50, 15852–15855.
25. Kandemir B; Chakraborty S; Guo Y; Bren KL Semisynthetic and Biomolecular Hydrogen Evolution Catalysts. Inorg. Chem 2015, 55, 467–477. [PubMed: 26671416]
26. Slater JW; Marguet SC; Cirino SL; Maugeri PT; Shafaat HS Experimental and DFT Investigations Reveal the Influence of the Outer Coordination Sphere on the Vibrational Spectra of Nickel-Substituted Rubredoxin, a Model Hydrogenase Enzyme. Inorg. Chem 2017, 56, 3926–3938. [PubMed: 28323426]
27. Kandemir B; Kubie L; Guo Y; Sheldon B; Bren KL Hydrogen Evolution from Water Under Aerobic Conditions Aatalyzed by a Cobalt ATCUN Metallopeptide. Inorg. Chem 2016, 55, 1355–1357. [PubMed: 26727542]
28. Dutta A; Hamilton GA; Hartnett HE; Jones AK Construction of Heterometallic Clusters in a Small Peptide Scaffold as [NiFe]-Hydrogenase Models: Development of a Synthetic Methodology. Inorg. Chem 2012, 51, 9580–9588. [PubMed: 22924594]
29. Roy S; Shinde S; Hamilton GA; Hartnett HE; Jones AK Artificial [FeFe]-Hydrogenase: On Resin Modification of an Amino Acid to Anchor a Hexacarbonyldiiron Cluster in a Peptide Framework. Eur. J. Inorg. Chem 2011, 2011, 1050–1055.
30. Jones AK; Lichtenstein BR; Dutta A; Gordon G; Dutton PL Synthetic Hydrogenases: Incorporation of an Iron Carbonyl Thiolate into a Designed Peptide. J. Am. Chem. Soc 2007, 129, 14844–14845. [PubMed: 17997557]
31. Onoda A; Kihara Y; Fukumoto K; Sano Y; Hayashi T Photoinduced Hydrogen Evolution Catalyzed by a Synthetic Diiron Dithiolate Complex Embedded Within a Protein Matrix. ACS Catal 2014, 4, 2645–2648.
32. Bacchi M; Berggren G; Niklas J; Veinberg E; Mara MW; Shelby ML; Poluektov OG; Chen LX; Tiede DM; Cavazza C Cobaloxime-Based Artificial Hydrogenases. Inorg. Chem 2014, 53, 8071–8082. [PubMed: 25029381]
33. Kleingardner JG; Kandemir B; Bren KL Hydrogen Evolution from Neutral Water Under Aerobic Conditions Catalyzed by Cobalt Microperoxidase-11. J. Am. Chem. Soc 2013, 136, 4–7. [PubMed: 24351231]
34. Saint-Martin P; Lespinat PA; Fauque G; Berlier Y; LeGall J; Moura I; Teixeira M; Xavier AV; Moura JJ Hydrogen Production and Deuterium-Proton Exchange Reactions Catalyzed by Desulfovibrio Nickel (II)-Substituted Rubredoxins. Proc. Natl. Acad. Sci 1988, 85, 9378–9380. [PubMed: 16594005]
35. Dutta A; DuBois DL; Roberts JA; Shaw WJ Amino Acid Modified Ni Catalyst Exhibits Reversible H_2 Oxidation/Production Over a Broad pH Range at Elevated Temperatures. Proc. Natl. Acad. Sci 2014, 111, 16286–16291. [PubMed: 25368196]
36. Dutta A; Lense S; Hou J; Engelhard MH; Roberts JA; Shaw WJ Minimal Proton Channel Enables H_2 Oxidation and Production with a Water-Soluble Nickel-Based Catalyst. J. Am. Chem. Soc 2013, 135, 18490–18496. [PubMed: 24206187]

37. Dutta A; Roberts JA; Shaw WJ Arginine-Containing Ligands Enhance H_2 Oxidation Catalyst Performance. Angew. Chem. Intl. Ed 2014, 53, 6487–6491.
38. Zhang W; Hong J; Zheng J; Huang Z; Zhou J; Xu R Nickel-Thiolate Complex Catalyst Assembled in One Step in Water for Solar H 2 Production. J. Am. Chem. Soc 2011, 133, 20680–20683. [PubMed: 22133284]
39. Vita N; Platsaki S; Basle A; Allen SJ; Paterson NG; Crombie AT; Murrell JC; Waldron KJ; Dennison C A Four-Helix Bundle Stores Copper for Methane Oxidation. Nature 2015, 525, 140–143. [PubMed: 26308900]
40. Leger C; Bertrand P Direct Electrochemistry of Redox Enzymes as a Tool for Mechanistic Studies. Chem. Rev 2008, 108, 2379–2438. [PubMed: 18620368]
41. Chakraborty S; Touw DS; Peacock AF; Stuckey J; Pecoraro VL Structural Comparisons of Apo- and Metalated Three-Stranded Coiled Coils Clarify Metal Binding Determinants in Thiolate Containing Designed Peptides. J. Am. Chem. Soc 2010, 132, 13240–13250. [PubMed: 20825181]
42. Phillips JC; Braun R; Wang W; Gumbart J; Tajkhorshid E; Villa E; Chipot C; Skeel RD; Kale L; Schulten K Scalable Molecular Dynamics with NAMD. J. Comput. Chem 2005, 26, 1781–1802. [PubMed: 16222654]
43. Denny JA; Darensbourg MY Metallodithiolates as Ligands in Coordination, Bioinorganic, and Organometallic Chemistry. Chem. Rev 2015, 115, 5248–5273. [PubMed: 25948147]
44. Colpas GJ; Kumar M; Day RO; Maroney MJ Structural Investigations of Nickel Complexes with Nitrogen and Sulfur Donor Ligands. Inorg. Chem 1990, 29, 4779–4788.
45. Moura I; Teixeira M; Moura JJ; LeGall J Spectroscopic Studies of Cobalt and Nickel Substituted Rubredoxin and Desulforedoxin. J. Inorg. Biochem 1991, 44, 127–139. [PubMed: 1664851]
46. Colpas GJ; Maroney MJ; Bagyinka C; Kumar M; Willis WS; Suib SL; Mascharak PK; Baidya N X-ray Spectroscopic Studies of Nickel Complexes, with Application to the Structure of Nickel Sites in Hydrogenases. Inorg. Chem 1991, 30, 920–928.
47. Ogata H; Hirota S; Nakahara A; Komori H; Shibata N; Kato T; Kano K; Higuchi Y Activation Process of [NiFe] Hydrogenase Elucidated by High-Resolution X-ray Analyses: Conversion of the Ready to the Unready State. Structure 2005, 13, 1635–1642. [PubMed: 16271886]
48. Gu Z; Dong J; Allan CB; Choudhury SB; Franco R; Moura JJ; Moura I; LeGall J; Przybyla AE; Roseboom W Structure of the Ni Sites in Hydrogenases by X-ray Absorption Spectroscopy. Species Variation and the Effects of Redox Poise. J. Am. Chem. Soc 1996, 118, 11155–11165.
49. Wang B; Shi Y; Tejero J; Powell SM; Thomas LM; Gladwin MT; Shiva S; Zhang Y; Richter-Addo GB Nitrosyl Myoglobins and their Nitrite Precursors: Crystal Structural and Quantum Mechanics and Molecular Mechanics Theoretical Investigations of Preferred Fe-NO Ligand Orientations in Myoglobin Distal Pockets. Biochemistry 2018, 57, 4788–4802. [PubMed: 29999305]
50. Creutz C; Sutin N; Brunschwig BS Excited-State Photochemistry in the Tris(2,2'-bipyridine)ruthenium(II)-Sulfite System. J. Am. Chem. Soc 1979, 101, 1297–1298.
51. Krishnan CV; Sutin N Homogeneous Catalysis of the Photoreduction of Water by Visible Light. 2. Mediation by a Tris(2,2'-bipyridine)ruthenium(II)-Cobalt(II) Bipyridine System. J. Am. Chem. Soc 1981, 103, 2141–2142.
52. McNamara WR; Han Z; Alperin PJ; Brennessel WW; Holland PL; Eisenberg R A Cobalt-Dithiolene Complex for the Photocatalytic and Electrocatalytic Reduction of Protons. J. Am. Chem. Soc 2011, 133, 15368–15371. [PubMed: 21863808]
53. McNamara WR; Han Z; Yin C-J; Brennessel WW; Holland PL; Eisenberg R Cobalt-Dithiolene Complexes for the Photocatalytic and Electrocatalytic Reduction of Protons in Aqueous Solutions. Proc. Natl. Acad. Sci 2012, 109, 15594–15599. [PubMed: 22691494]
54. Brown GM; Chan S; Creutz C; Schwarz HA; Sutin N Mechanism of the Formation of Dihydrogen from the Photoinduced Reactions of Tris (bipyridine) Ruthenium (II) with Tris (bipyridine) Rhodium (III). J. Am. Chem. Soc 1979, 101, 7638–7640.
55. del Barrio M; Sensi M; Orain C; Baffert C; Dementin S; Fourmond V; Leger C Electrochemical Investigations of Hydrogenases and Other Enzymes that Produce and Use Solar Fuels. Acc. Chem. Res 2018, 51, 769–777. [PubMed: 29517230]
56. Leger C; Bertrand P Direct Electrochemistry of Redox Enzymes as a Tool for Mechanistic Studies. Chem. Rev 2008, 108, 2379–2438. [PubMed: 18620368]

57. Armstrong FA; Evans RM; Hexter SV; Murphy BJ; Roessler MM; Wulff P Guiding Principles of Hydrogenase Catalysis Instigated and Clarified by Protein Film Electrochemistry. Acc. Chem. Res 2016, 49, 884–892. [PubMed: 27104487]
58. Armstrong FA Insights from Protein Film Voltammetry into Mechanisms of Complex Biological Electron-Transfer Reactions. Dalton Trans 2002, 661–671.
59. Leger C; Jones AK; Albracht SP; Armstrong FA Effect of a Dispersion of Interfacial Electron Transfer Rates on Steady State Catalytic Electron Transport in [NiFe]-Hydrogenase and Other Enzymes. J. Phys. Chem. B 2002, 106, 13058–13063.
60. Leger C; Jones AK; Roseboom W; Albracht SP; Armstrong FA Enzyme Electrokinetics: Hydrogen Evolution and Oxidation by *Allochromatium vinosum* [NiFe]-Hydrogenase. Biochemistry 2002, 41, 15736–15746. [PubMed: 12501202]
61. Fourmond V; Baffert C; Sybirna K; Lautier T; Abou Hamdan A; Dementin S; Soucaille P; Meynial-Salles I; Bottin H; Leger C Steady-State Catalytic Wave-Shapes for 2- Electron Reversible Electrocatalysts and Enzymes. J. Am. Chem. Soc 2013, 135, 3926–3938. [PubMed: 23362993]
62. Fourmond V; Leger C Modelling the Voltammetry of Adsorbed Enzymes and Molecular Catalysts. Curr. Opin. Electrochem 2017, 1, 110–120.
63. Thoi VS; Sun Y; Long JR; Chang CJ Complexes of Earth-Abundant Metals for Catalytic Electrochemical Hydrogen Generation under Aqueous Conditions. Chem. Soc. Rev 2013, 42, 2388–2400. [PubMed: 23034627]
64. Michel LV; Ye T; Bowman SEJ; Levin BD; Hahn MA; Russell BS; Elliott SJ; Bren KL Heme Attachment Motif Mobility Tunes Cytochrome c Redox Potential. Biochemistry 2007, 46, 11753–11760. [PubMed: 17900177]
65. Dey S; Rana A; Dey SG; Dey A Electrochemical Hydrogen Production in Acidic Water by an Azadithiolate Bridged Synthetic Hydrogenese Mimic: Role of Aqueous Solvation in Lowering Overpotential. ACS Catal 2013, 3, 429–436.
66. Riddles PW; Blakeley RL; Zerner B Ellman's Reagent: 5, 5-Dithiobis (2-Nitrobenzoic Acid) ~a Reexamination. Anal. Biochem 1979, 94, 75–81. [PubMed: 37780]
67. Greenfield NJ Using Circular Dichroism Collected as a Function of Temperature to Determine the Thermodynamics of Protein Unfolding and Binding Interactions. Nat. Prot 2006, 1, 2527–2535.
68. Ravel B; Newville M ATHENA, ARTEMIS, HEPHAESTUS: Data Analysis for X-ray Absorption Spectroscopy using IFEFFIT. J. Synchrotron Radiat 2005, 12, 537–541. [PubMed: 15968136]
69. Gaussian Program, Frisch MJ; Trucks GW; Schlegel HB; Scuseria GE; Robb MA; Cheeseman JR; Scalmani G; Barone V; Mennucci B; Petersson GA; Nakatsuji H; Caricato M; Li X; Hratchian HP; Izmaylov AF; Bloino J; Zheng G; Sonnenberg JL; Hada M; Ehara M; Toyota K; Fukuda R; Hasegawa J; Ishida M; Nakajima T; Honda Y; Kitao O; Nakai H; Vreven T; Montgomery JA Jr.; Peralta JE; Ogliaro F; Bearpark M; Heyd JJ; Brothers E; Kudin KN; Staroverov VN; Keith T; Kobayashi R; Normand J; Raghavachari K; Rendell A; Burant JC; Iyengar SS; Tomasi J; Cossi M; Rega N; Millam JM; Klene M; Knox JE; Cross JB; Bakken V; Adamo C; Jaramillo J; Gomperts R; Stratmann RE; Yazyev O; Austin AJ; Cammi R; Pomelli C; Ochterski JW; Martin RL; Morokuma K; Zakrzewski VG; Voth GA; Salvador P; Dannenberg JJ; Dapprich S; Daniels AD; Farkas O; Foresman JB; Ortiz JV; Cioslowski J; Fox DJ; Gaussian 09, Revision D.01; Gaussian, Inc.: Wallingford CT, 2013.
70. Becke AD Density-Functional Thermochemistry. III. The Role of Exact Exchange. J. Chem. Phys 1993, 98, 5648–5652.
71. Lee C; Yang W; Parr RG Development of the Colle-Salvetti Correlation-Energy Formula into a Functional of the Electron Density. Phys. Rev. B 1988, 37, 785–789.
72. Vreven T; Byun KS; Komaromi I; Dapprich S; Montgomery JA; Morokuma K; Frisch MJ Combining Quantum Mechanics Methods with Molecular Mechanics Methods in ONIOM. J. Chem. Theory Comput 2006, 2, 815–826. [PubMed: 26626688]
73. Torrent M; Vreven T; Musaev DG; Morokuma K; Farkas O; Schlegel HB Effects of the Protein Environment on the Structure and Energetics of Active Sites of Metalloenzymes. ONIOM Study of Methane Monooxygenase and Ribonucleotide Reductase. J. Am. Chem. Soc 2002, 124, 192–193. [PubMed: 11782169]

74. Chung LW; Li X; Sugimoto H; Shiro Y; Morokuma K ONIOM Study on a Missing Piece in our Understanding of Heme Chemistry: Bacterial Tryptophan 2,3-Dioxygenase with Dual Oxidants. J. Am. Chem. Soc 2010, 132, 11993–12005. [PubMed: 20698527]

75. Kawatsu T; Lundberg M; Morokuma K Protein Free Energy Corrections in ONIOM QM:MM Modeling: A Case Study for Isopenicillin N Synthase (IPNS). J. Chem. Theory Comput 2011, 7, 390–401. [PubMed: 26596161]

76. Cornell WD; Cieplak P; Bayly CI; Gould IR; Merz KM; Ferguson DM; Spellmeyer DC; Fox T; Caldwell JW; Kollman PA A Second Generation Force Field for the Simulation of Proteins, Nucleic Acids, and Organic Molecules. J. Am. Chem. Soc 1995, 117, 5179–5197.

77. Singh UC; Kollman PA An Approach to Computing Electrostatic Charges for Molecules. J. Comput. Chem 1984, 5, 129–145.

78. Lill SON; Siegbahn PEM An Autocatalytic Mechanism for NiFe-Hydrogenase: Reduction to Ni(I) Followed by Oxidative Addition. Biochemistry 2009, 48, 1056–1066. [PubMed: 19138102]

79. Fourmond V QSoas: A Versatile Software for Data Analysis. Anal. Chem 2016, 88, 5050–5052. [PubMed: 27096413]

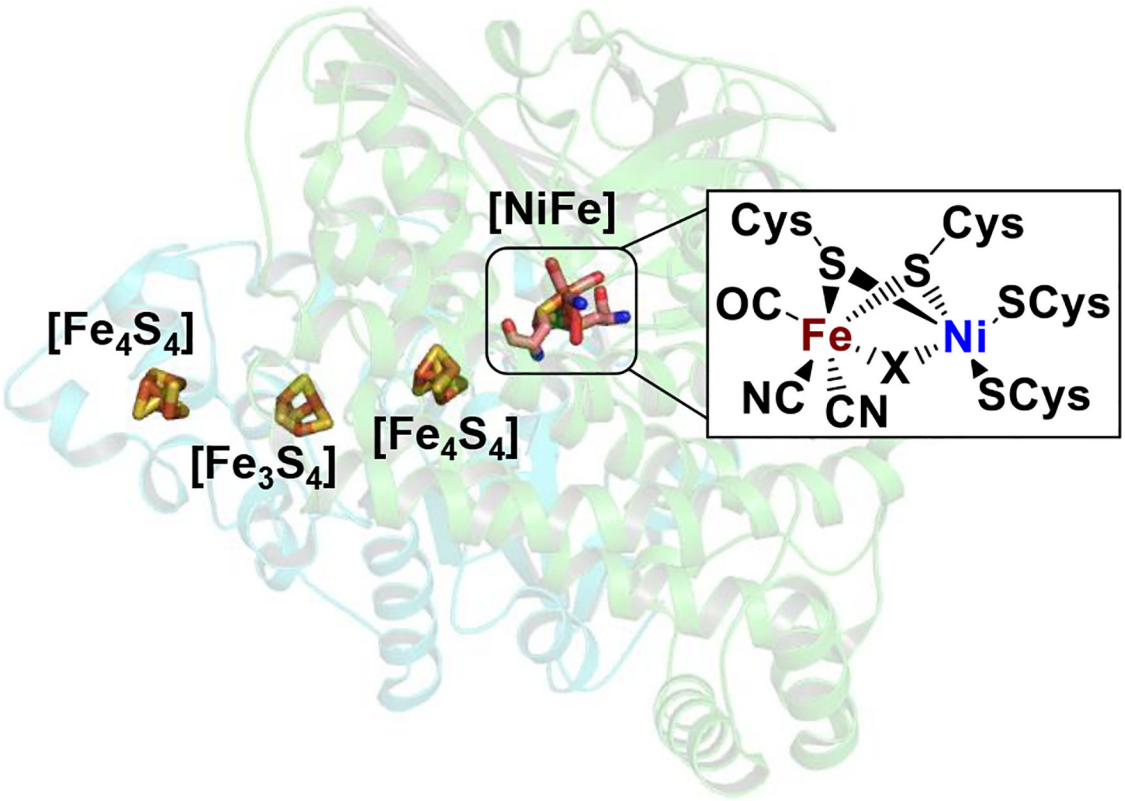

Figure 1.

Overall structure of *Desulfovibrio vulgaris* [NiFe] hydrogenase (PDB: 1WUI). The coordination environment of the binuclear active site in the large subunit (green cartoon) is drawn on the right. The Fe-S sites in the small subunit (cyan cartoon) are shown as stick models. Figure made in PyMoL.

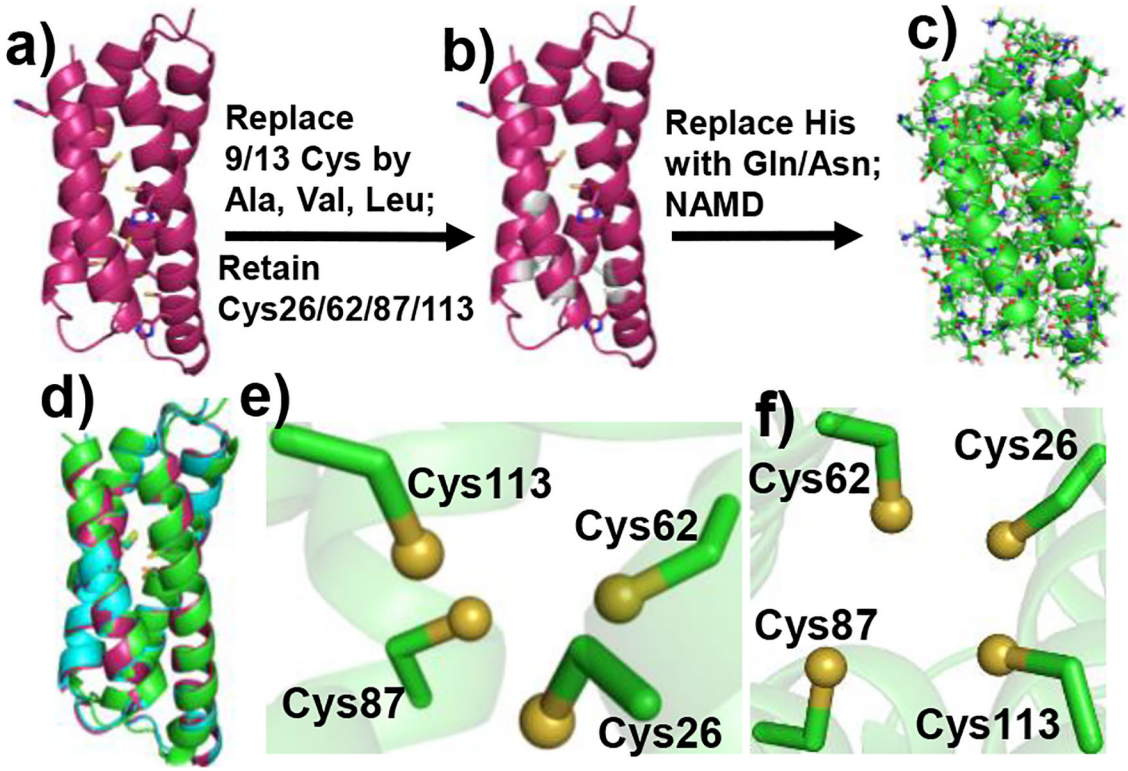

Figure 2.

Redesign approach of Csp1 (a-b) to NBP. c) NAMD model of apo NBP. d) Overlay of X-ray structures of apo Csp1 (purple; PDB: 5FJD), Cu(I)-Csp1 (cyan; PDB: 5FJE), and minimized structure of apo NBP (green). Ball and stick model of the tetrathiolate site of minimized NBP viewed perpendicular to the helical axis (e), and from the top of the helical axis (f) with N- terminus at the top. Modeling performed using CHARMM22 force fields.

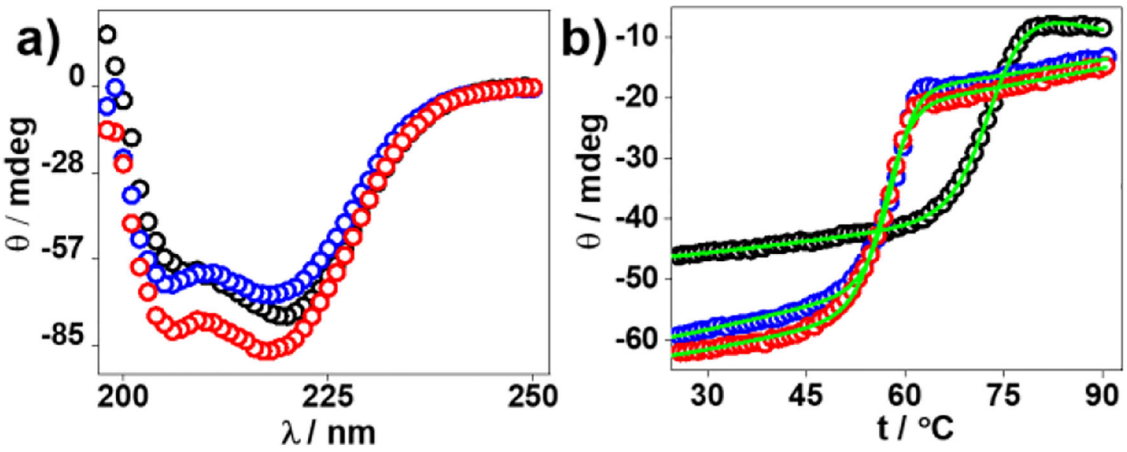

Figure 3.

a) CD and b) thermal melts monitored at λ_{222} of 3.5 μM apo NBP (blue), Ni(II)-NBP (red), and apo CspI (black) in 5 mM Tris buffer pH 8.5. Green lines in b represent fits to the experimental data using the Gibbs-Helmholtz equation to derive T_m, ΔH^{unfold} and $\Delta C^{punfold}$ shown in Table 1. All experiments were performed with reduced proteins placed in the CD chamber where a constant flow of N_2 gas was maintained throughout the experiments.

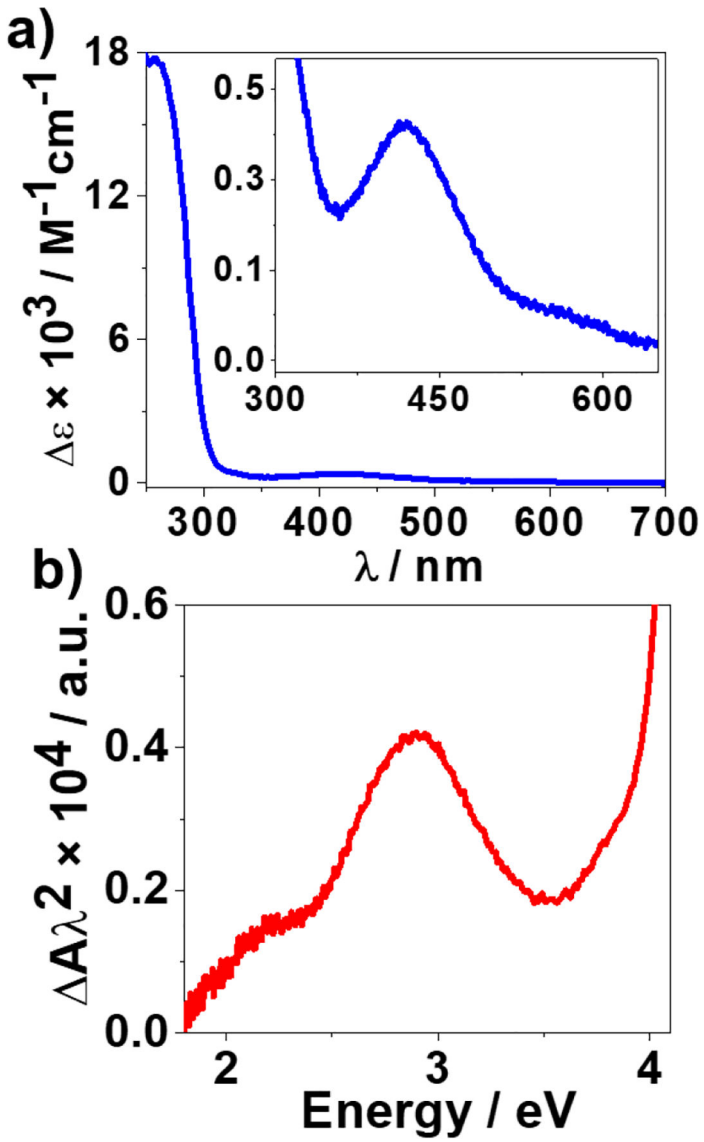

Figure 4.

a) UV-vis difference spectrum of 50 μM Ni(II)-NBP subtracted from apo NBP in 50 mM Tris buffer pH 8.5. Inset shows the 300–700 nm region of the spectrum. b) A photon energy plot of the 300–700 nm region of the UV-vis data showing more resolved features for the 327 nm (3.79 eV), and 566 nm (2.19 eV) peaks.

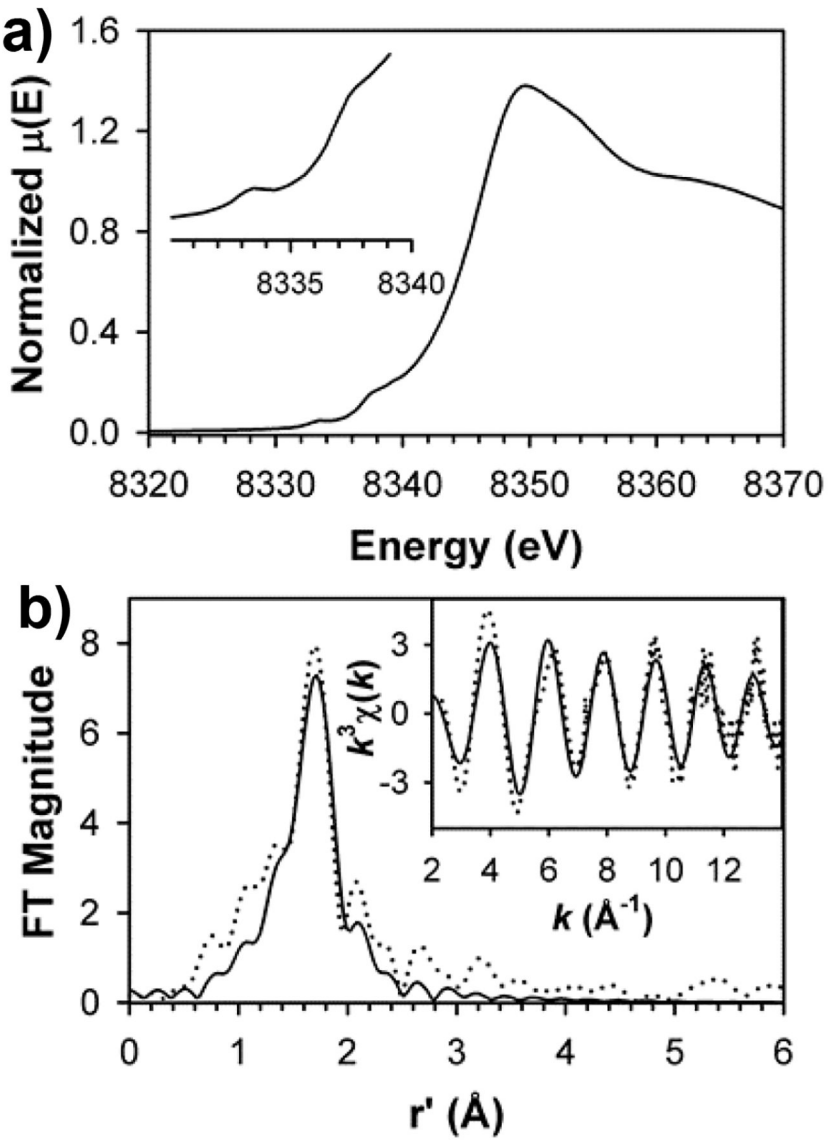

Figure 5.

a) Normalized XANES spectrum of Ni(II)-NBP. The inset depicts an expansion of the pre-edge region. b) Best first-shell fit to k^3-weighted EXAFS data of Ni(II)-NBP. Experimental data is shown as dotted lines, while the best fits are shown as solid lines.

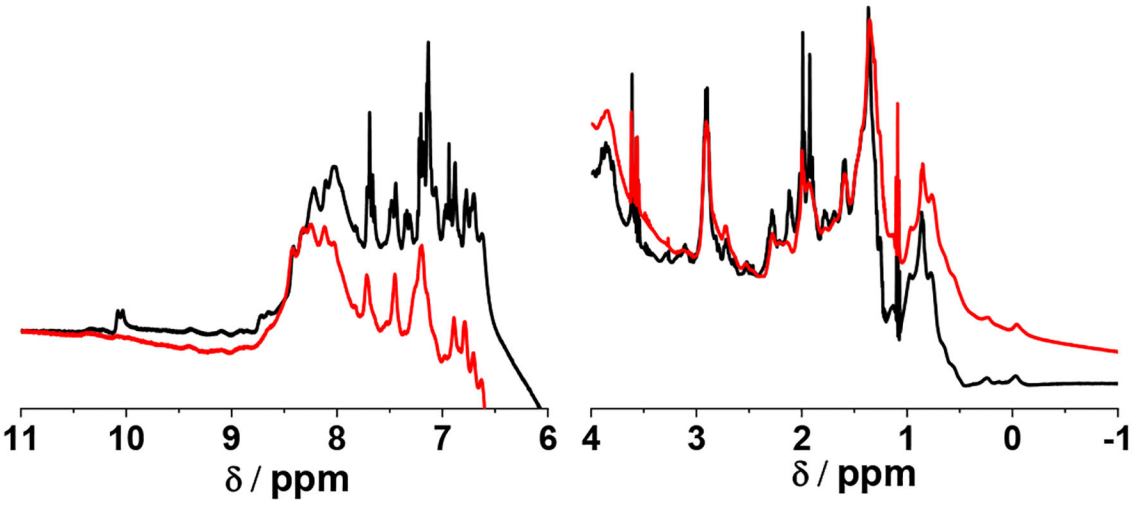

Figure 6.

^{1}H NMR spectra of 400 μM apo (black), and Ni-NBP (red) in 0.1 M phosphate buffer pH 8.1 containing 0.1 M NaCl in 10% D_2O Shown are the aromatic (left) and aliphatic (right) regions of the spectra. The water peak is omitted for clarity.

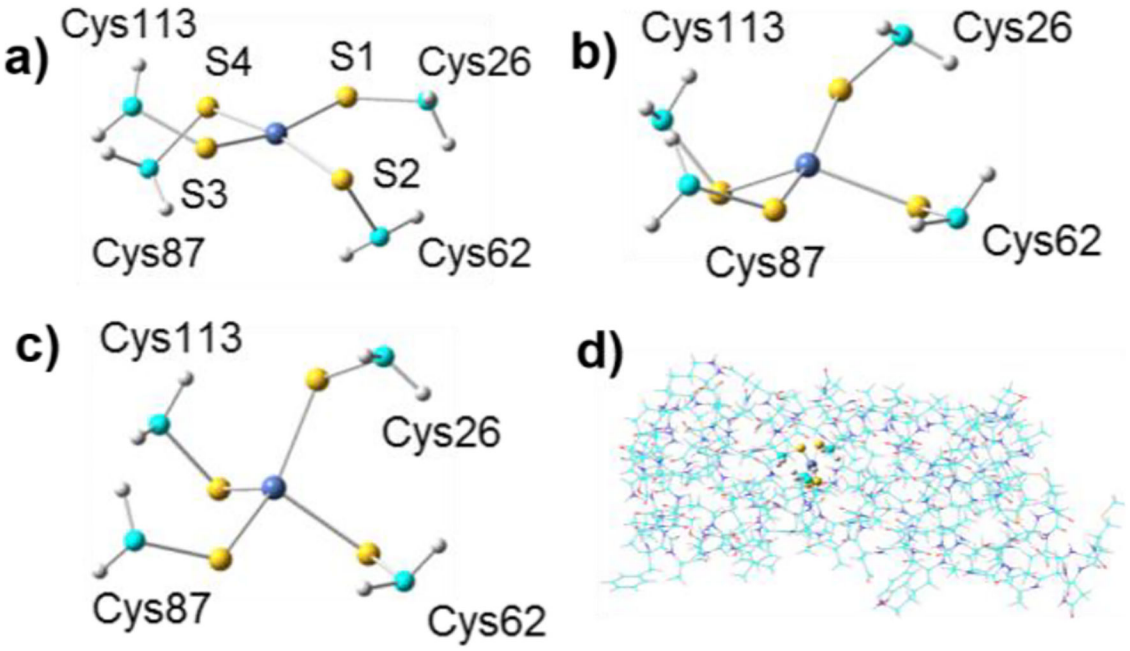

Figure 7.

QM regions of optimized NBP models (a) ^{1}NBP-SP; (b) ^{1}NBP-TH; (c) ^{3}NBP-TH; (d) the lowest energy QM/MM NBP model. Atom color scheme: Ni- light blue; S- yellow; C- cyan; H- gray.

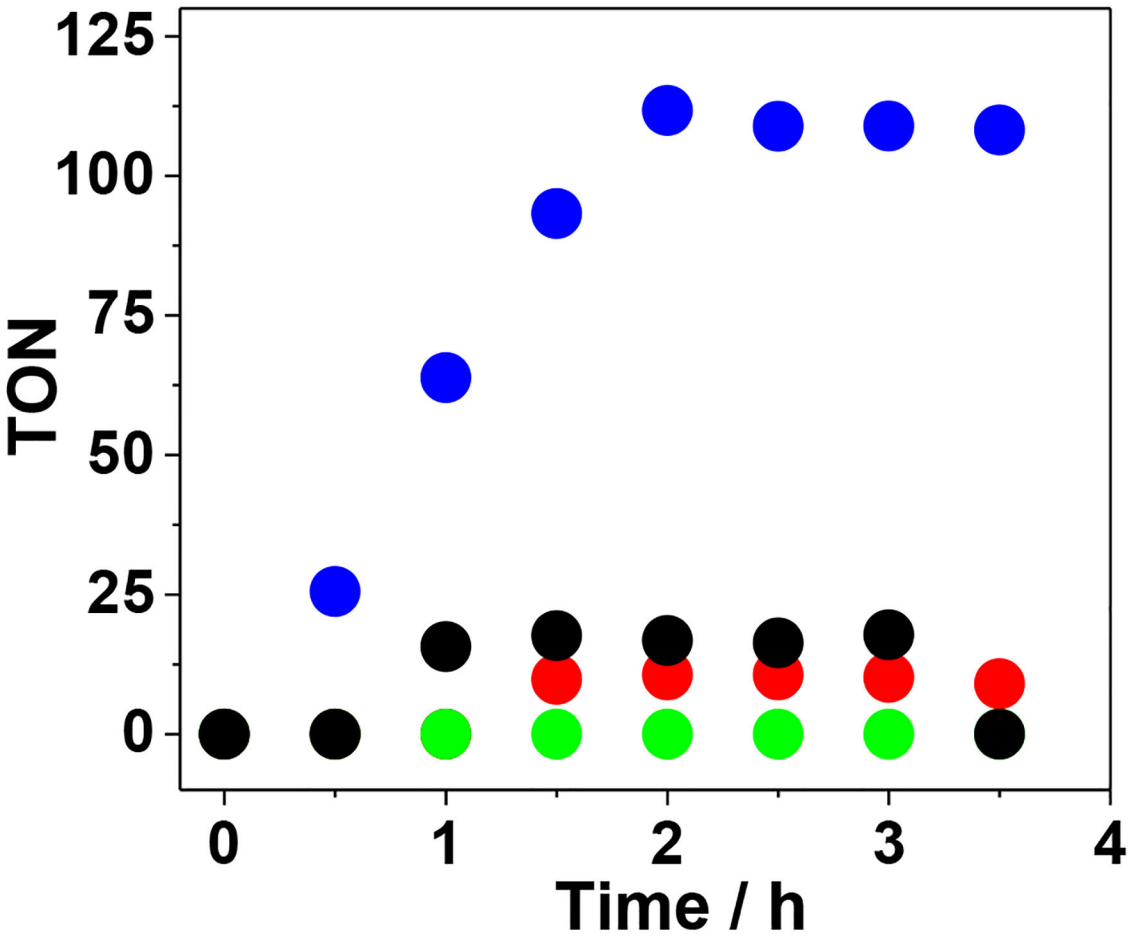

Figure 8.

TON for H_2 production under photochemical conditions. The anaerobically prepared samples contained 2 μM proteins, 100 mM ASC, 1 mM $Ru(bpy)_3^{2+}$ in 1 M phosphate buffer pH 7 and irradiated using a white LED (λ>400 nm) power source adjusted to 180 mW placed at 30 cm from the sample. Blue: Ni(II)-NBP; red: apo NBP; green: Ni(II)-NBP in the absence of photosensitizer; black: 2 |iM NiSO4. Note: Some data points are overlapping.

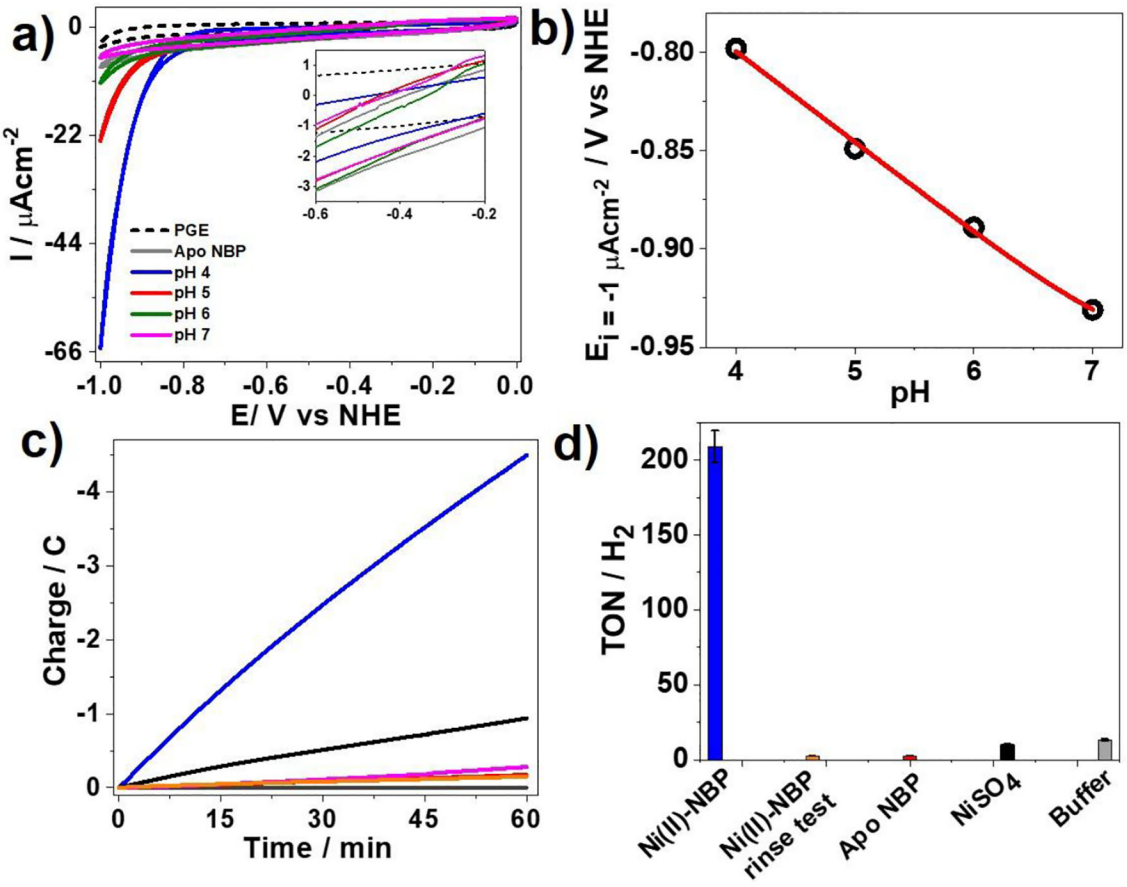

Figure 9.

pH dependent CVs of 170 μM Ni(II)-NBP adsorbed on PGE in N2 saturated mixed buffers (scan rate =10 mV/s) at 15°C. PGE and apo NBP are at pH 4. b) Pourbaix diagram showing dependence of redox potentials $E_{i=-1\mu A/cm2}$ obtained from anodic and cathodic wave averaged catalytic voltammograms vs pH. The red line represents a fit to the data using the equation vi. c) Charge passed in Coulombs during 1 h of CPE of 7 mL solutions of 25 μM Ni(II)-NBP (blue), Ni(II)-NBP after rinse test (orange), apo NBP (red), $NiSO_4$ (black), and buffer alone (gray) using a 3 mm graphite electrode polarized at −1V vs NHE. All CPE were performed at pH 5. d) TON for H_2 production of the corresponding samples from CPE experiments in c. 250 μL of the headspace gas from the CPE experiments were injected into the GC and the TON was calculated from observed raw signals accordingly (see Materials and Methods). Error bars from 2–3 independent measurements. Data were collected against Ag/AgCl reference and converted to NHE using $E_{NHE} = E_{Ag/AgCl} + 0.197$. Although the data in 9a were collected with an electrode rotation rate of 2000 rpm, the current was not found to be rotation rate-dependent.

Table 1.

Parameters derived from the data in Figure 3.

Sample	% α-helix[a]	T_m (°C)[b]	ΔH^{unfold} (kcal/mol)[b]	ΔCp^{unfold} (kcal/mol/k)[b]
Apo NBP	42	58	110	4.6
Ni(II)-NBP	53	58	100	4.2
Apo-Csp1	48	73	82	2.2

[a] From Figure 3a, and

[b] from the Gibbs-Helmholtz analysis of Figure 3b.

Author Manuscript

Author Manuscript

Author Manuscript

Table 2.

UV-vis spectral parameters of Ni(II)-NBP.

Sample	λ / nm	eV	Δε $M^{-1}cm^{-1}$
Ni(II)-NiBP	256	4.84	17,740
	327	3.79	420
	420	2.95	400
	566	2.19	87